Supplementary Information for

Unlocking high-current-density nitrate reduction and formaldehyde oxidation synergy for scalable ammonia production and fixation

Linjie Zhang,[‡a] Yimeng Cai,[‡a] Yanghua Li,[a] Chen Sun,[a] Yi Xiao,[a] Yibing Yang,[a] Dechao Chen,[a] Dongdong Xiao,[b] Chi-Feng Lee,[c] Yunjian Wang,[a] Shiqiang Feng,[a] Hsiao-Tsu Wang,[c] Yu-Cheng Shao,[d] Ting-Shan Chan,[d] Hirofumi Ishii,[d] Nozomu Hiraoka,[d] Xiuyun Wang,[e] Jun Luo[f] and Lili Han*[a]

[a]State Key Laboratory of Structural Chemistry, Fujian Institute of Research on the Structure of Matter, Chinese Academy of Sciences, Fuzhou 350002, China

[b]Beijing National Laboratory for Condensed Matter Physics, Institute of Physics, Chinese Academy of Sciences, Beijing 100190, China

[c]Department of Physics, Tamkang University, New Taipei City 251301, Taiwan

[d]National Synchrotron Radiation Research Center, Hsinchu 300092, Taiwan

[e]National Engineering Research Center of Chemical Fertilizer Catalyst, Fuzhou University, Fuzhou 350002, China

[f]ShenSi Lab, Shenzhen Institute for Advanced Study, University of Electronic Science and Technology of China, Longhua District, Shenzhen 518110, China

[‡]These authors contributed equally to this work.

*To whom correspondence may be addressed. Email: llhan@fjirsm.ac.cn

This PDF file includes:

- Supplementary text
- Figs. S1 to S54
- Note S1
- Tables S1 to S10
- References (1 to 32)

Other supplementary materials for this manuscript include the following:

- Movie S1
- Movie S2

Supplementary Information Text

Chemicals and reagents

Potassium hydroxide (KOH, 95%), sodium hypochlorite standard solution (NaClO, 0.1 M), deuterium oxide (D_2O, 99.9 atom%), potassium nitrate-^{15}N ($K^{15}NO_3$, 99 atom%, ≥98.5%), ammonium-^{15}N chloride ($^{15}NH_4Cl$, 99 atom%, ≥98%), dimethyl sulfoxide (DMSO, ≥99.9%, HPLC), 5,5-dimethyl-1-pyrroline-N-oxide (DMPO, 97%), formate (HCOOH, 98%), 5-(hydroxymethyl)furfural (HMF, $C_6H_6O_3$, ≥95%), 2,5-furandicarboxylic acid (FDCA, $C_6H_4O_5$, 98%), 4-pyridinecarboxaldehyde (4-PCA, C_6H_5NO, 99%), and isonicotinic acid (INA, $C_6H_5NO_2$, 99%) were purchased from Shanghai Macklin Biochemical Co., Ltd. Potassium nitrate (KNO_3, 99%), hydrochloric acid (HCl, 36.0%-38.0%, AR), sulfuric acid (H_2SO_4, 98%, AR), sodium hydroxide (NaOH, 97%), ammonium persulfate ($(NH_4)_2S_2O_8$, 98%), formaldehyde solution (HCHO, 40%, AR), absolute ethanol (C_2H_5OH, AR), chloroform ($CHCl_3$, AR) were procured from Sinopharm Chemical Reagent Co., Ltd. Silver nitrate ($AgNO_3$, 99%), sodium nitroferricyanide ($C_5FeN_6Na_2O$, 99.0%), sodium citrate ($C_6H_5Na_3O_7$, 99.0%), salicylic acid ($C_7H_6O_3$, 99.5%) and phosphoric acid (H_3PO_4, AR) were sourced from Aladdin Chemical Co., Ltd. Cu foams (thickness: 1 mm) were acquired from Williek photoelectric materials Co., Ltd. Ultrapure water (18.25 MΩ cm) from a Water Purifier System was used throughout the experiments.

Materials and Methods

Synthesis of $Cu(OH)_2$ nanowires ($Cu(OH)_2$ NWs)

Cu foam (1×2.5 cm^2) was pretreated by sonication with anhydrous ethanol, water and 1 M HCl solution for 10 min each. Then it was submerged in a 30 mL of mixed solution containing 0.05 M $(NH_4)_2S_2O_8$ and 1 M NaOH, and left to stand for various durations before being rinsed three times with anhydrous ethanol and blown dried with cold air to obtain the blue $Cu(OH)_2$ nanowires. Samples obtained after soaking for 10, 20, 30, and 40 min are designated as $Cu(OH)_2$ NWs-1, $Cu(OH)_2$ NWs-2, $Cu(OH)_2$ NWs-3, and $Cu(OH)_2$ NWs-4, respectively.

Synthesis of $Ag_1@Cu(OH)_2$ NWs

$Cu(OH)_2$ NWs-4 was immersed in a 5 mL aqueous solution containing 1.5 mM $AgNO_3$ for 1 h. Subsequently, it was washed three times with anhydrous ethanol, dried by blowing air, and thus, the $Ag_1@Cu(OH)_2$ NWs were obtained.

Synthesis of $Ag_1@Cu_2O$ NWs

The $Ag_1@Cu(OH)_2$ NWs were subjected to a heat treatment at 200 °C for 1 h in a tube furnace under an H_2/Ar atmosphere (with a H_2 content of 5%), and the $Ag_1@Cu_2O$ NWs were obtained.

Synthesis of Cu_2O NWs

The obtained $Cu(OH)_2$ NWs-4 sample was loaded into a tube furnace and subjected to heating at a ramping rate of 1 °C min^{-1} under an H_2/Ar atmosphere (with H_2 content of 5%). Subsequently, it was maintained at 200 °C for 1 h to obtain the Cu_2O NWs.

Physical characterizations

Powder X-ray diffraction (XRD) patterns were recorded using a Rigaku Miniflex 600 diffractometer with Cu K_α radiation in the 2ϑ range of 20° to 70°. Scanning electron microscopy (SEM) images were taken using a Hitachi SU8010 Scanning Electron Microscope. High-resolution transmission electron microscopy (HRTEM), aberration-corrected high-angle annular dark-field scanning TEM (AC-HAADF-STEM) images, and energy-dispersive X-ray spectroscopy (EDS) maps were acquired using a JEOL JEM-ARM300F transmission electron microscope. High-resolution electron energy loss spectroscopy (EELS) mapping was performed with a field-emission TEM (JEOL JEM-F200) at 200 kV. Inductively coupled plasma optical emission spectroscopy (ICP-OES) was employed to quantitatively determine the metal contents of Cu and Ag using a Perkin Elmer Avio 200 ICP optical emission spectrometer. X-ray photoelectron spectroscopy (XPS) analysis was conducted using a Thermo Fisher Scientific Escalab 250Xi photoelectron spectrometer. Ex-situ X-ray absorption fine structure (XAFS) spectra at the Cu *K*-edge and Ag *K*-edge were measured on beamline TLS 01C1 in a fluorescence mode at the National Synchrotron Radiation Research Center, with data processing using the Athena program. Ultraviolet-visible (UV-vis) absorbance data were collected using a Perkin Elmer Lambda 950 spectrophotometer. Liquid products were analyzed using a proton nuclear magnetic resonance (^{1}H NMR) spectrometer (Bruker Advance Neo 600 MHz). Gaseous products were analyzed online using as a gas chromatograph (Fuli GC9790PLUS) equipped with a thermal conductivity detector (TCD).

Electrochemical measurements

A CHI-1100C potentiostat (Shanghai Chenhua, China) coupled with a DuPont Nafion 117 membrane-separated H-cell was utilized. The Cu foam-backed samples served directly as the working electrode, with a practical immersing area of 1 × 1 cm^2 in the electrolyte. Hg/HgO (1 M KOH) was used as the reference electrode, and positioned within the same chamber as the working electrode, while a Pt foil (1 × 1 cm^2) served as the counter electrode in the other chamber. The measured potentials were referenced to the reversible hydrogen electron (RHE) calculated using the Nernst equation: $E_{\mathrm{RHE}} = E_{\mathrm{Hg/HgO}} + 0.059 \times \mathrm{pH} + 0.098$ V. **All reported potentials were not *iR*-drop compensated.**

For the electrocatalytic nitrate reduction reaction (NO_3^-RR) experiments, 25 mL of 1 M KOH containing KNO_3 at specific concentrations of 10, 100, 250, and 500 mM were used as the catholyte, while 25 mL of 1 M KOH solution served as the anolyte. The tail gas generated during the experiment was captured using 50 mL of 0.5 M H_2SO_4 solution. For the electrocatalytic formaldehyde oxidation reaction (FOR), 25 mL of 1 M KOH containing HCHO at specific concentrations of 0.1, 0.2, 0.5, and 1 M were used as the anolyte, while 25 mL of 1 M KOH solution acted as the catholyte. Prior to the electrochemical measurements, the catholyte was saturated with high-purity Ar for 30 min to eliminate N_2/O_2 interference. Throughout the measurements, the KNO_3-contained catholyte and HCHO-contained anolyte were stirred at 500 rpm and continuously purged with high-purity Ar. Cyclic voltammetry (CV) was initially performed at a scan rate of 50 mV s^{-1} to activate the working electrode until stable currents were reached. Linear sweep voltammetry (LSV) curves were recorded at a scan rate of 5 mV s^{-1}. *I*–*t* tests were carried out at various potentials for a duration of 1 h. Electrochemical impedance spectroscopy (EIS) was operated at 0 V vs. RHE with an amplitude of 5 mV and a frequency range spanning from 10^6 to 10^{-2} Hz.

Paired NO_3^-RR/FOR electrolysis in membrane electrode assembly (MEA) electrolyzer

In the MEA electrolyzer, the $Ag_1@Cu_2O$ NWs electrode (with an effective area of 1 × 1 cm^2) served as both the cathode and anode for NO_3^-RR and FOR, respectively. An anion exchange membrane (AEM, FAA-3-50 FuMA-Tech) was separated between the anode and cathode compartments. During testing, the catholyte (1 M KOH + 0.1 M KNO_3) and anolyte (1 M KOH + 0.8 M HCHO) were continuously delivered into respective chambers at a flow rate of 3 mL min^{-1} using a two-channel peristaltic pump (BT100-3J, Longer) connected to silicone tubes (inner Φ = 3 mm). The MEA electrolyzer was operated at constant voltage for a predetermined duration, then the products from both sides were extracted for further analysis and treatment.

The experiments conducted using NO_3^-RR/4-PCAOR (anodic 4-PCA oxidation reaction) and NO_3^-RR/HMFOR (anodic HMF oxidation reaction) followed similar procedures to those described above for NO_3^-RR/FOR, except for the anolyte used. Specifically, the anolytes were respectively composed of 1 M KOH + 0.05 M 4-PCA and 1 M KOH + 0.05 M HMF, while all other conditions remained identical.

Ammonium acid salt products isolation

Ammonium formate ($HCOONH_4$): A straightforward chemical route involving stepwise acid neutralization, distillation, and rotary evaporation, was employed to chemically combine the NH_3 and formate products respectively from the cathodic and anodic chambers into high-purity $HCOONH_4$ solids. Specifically, the catholyte and anolyte post-electrolysis were mixed in a molar ratio of 1:1 of NH_3 to formate, followed by adjusting the pH of the combined electrolyte to 6 using a 1 M H_2SO_4 solution. At this stage, the combined electrolyte contained both $HCOONH_4$ product and K_2SO_4 byproduct through the following chemical reaction: $KOH + NH_3 + KCOOH + H_2SO_4 \rightarrow HCOONH_4 + K_2SO_4 + H_2O$. Subsequently, the $HCOONH_4$ aqueous solution and K_2SO_4 solid can be separated through high-temperature distillation. Following this, the distilled $HCOONH_4$ aqueous solution underwent further processing using a low-temperature rotary evaporator to obtain the $HCOONH_4$ solid.

Ammonium furandicarboxylic acid: The FDCA powder was easily obtained by acidifying the anolyte post-electrolysis using 1 M H_2SO_4 to induce the precipitation of the FDCA product, followed by filtration and vacuum drying. Subsequently, the FDCA powder was dissolved again in the catholyte post-electrolysis. After sequential acid neutralization using a 1 M H_2SO_4 solution and high-temperature distillation, the pure aqueous solution of ammonium furandicarboxylic acid and solid K_2SO_4 can be separated.

Ammonium isonicotinic acid: The INA powder was easily obtained by acid neutralization of the anolyte post-electrolysis using 1 M H_2SO_4, followed by chloroform ($CHCl_3$) extraction and vacuum drying. Subsequently, the INA powder was dissolved again in the catholyte post-electrolysis. After sequential acid neutralization using a 1 M H_2SO_4 solution and high-temperature distillation, the pure aqueous solution of ammonium isonicotinic acid and solid K_2SO_4 can be separated.

In-situ XAFS, in-situ ATR-FTIR, online DEMS and quasi-in-situ EPR measurements

All in-situ spectroscopic measurements were conducted using a three-electrode Teflon electrochemical cell containing electrolyte of 1 M KOH and 0.1 M KNO_3, with $Ag_1@Cu_2O$ NWs, Pt wire and Ag/AgCl electrode serving as the working, counter and reference electrodes, respectively.

Electrochemical in-situ XAFS measurements at the Cu *K*-edge and Ag *K*-edge were carried out at BL12B2 beamline at SPring-8, JARSI. In-situ XAFS signals were collected in fluorescence mode and recorded at operating potentials in a decreasing sequence, starting from open circuit potential (OCP) and then 0, −0.2, and finally −0.4 V vs. RHE, respectively. Before the signal collection, a potentiostatic operation was performed at each potential for 5 min.

In-situ attenuated total reflection Fourier-transform infrared spectroscopy (ATR-FTIR) measurements were performed with a Bruker INVENIO instrument. The ATR technique used a single bounce silicon crystal covered with an Au membrane in internal reflection mode. To prepare the catalyst ink, $Ag_1@Cu_2O$ NWs were dispersed ultrasonically in 500 μL of H_2O and 450 μL of ethanol for 45 min, followed by mixing it with 40 μL of 5% Nafion solution. Subsequently, the ink was added dropwise onto the Au membrane and dried naturally as a working electrode, with the electrolyte fed with Ar gas for 30 min prior to measurement. The background spectrum was acquired under open circuit potential (OCP), while other spectra were collected within the potential range from OCP to −0.4 V vs. RHE.

Online differential electrochemical mass spectrometry (DEMS) measurement was carried out using QAS 100 device (Linglu Instruments, Shanghai) to detect the reaction intermediates. During the LSV scanning from 0 to −0.4 V vs. RHE at a scan rate of 10 mV s^{-1}, continuous mass signal collection was conducted while Ar bubbling was maintained in the electrolyte. To ensure accuracy, three additional cycles were executed under identical conditions once the mass signal returned to baseline.

Quasi-in-situ electron paramagnetic resonance (EPR) spectra were recorded on a Bruker EPR-300 spectrometer. Typically, the electrocatalytic test was conducted at −0.1 V vs. RHE for a duration of 3 min. Subsequently, 0.2 mL of the *H trapping reagent, specifically DMPO, was added into the electrolyte and stirred for another 1 min before capturing the *H signals.

Determination of NH_3

The concentration of NH_3 produced was spectrophotometrically determined using the modified indophenol blue method. Color developer A was configured by dissolving 5 g of salicylic acid and 5 g of sodium citrate in 100 mL of 1 M NaOH solution. Oxidizer B consisted of the 0.05 M NaClO solution. Catalyst C was configured by dissolving 0.2 g of sodium nitroferricyanide in 20 mL of deionized water. To measure the NH_3 concentration, a certain amount of electrolyte was extracted from the electrolytic cell and diluted within the detection range in a colorimetric tube. Then, 2 mL of color developer A, 1 mL of oxidant B and 0.2 mL of catalyst C were sequentially added while shaking well before leaving it for 1 h in darkness. Afterwards, the absorbance was measured using a UV-vis spectrometer (peak absorption at λ = 655 nm). The NH_3 concentration–absorbance standard curve was made using a series of standard NH_4Cl solutions (see Fig. S12).

Determination of nitrite (NO_2^-)

The concentration of NO_2^- produced was determined by spectrophotometry. A color developer was prepared by thoroughly mixing 0.2 g of N-(1-naphthyl) ethylenediamine dihydrochloride, 4 g of p-aminobenzenesulfonamide, and 10 mL of phosphoric acid in 50 mL of deionized water. Then, 5 mL of the diluted electrolyte was added into a colorimetric tube, followed by the addition of 0.1 mL of color developer, and thorough mixing. After incubating at room temperature for 20 min, the absorption spectrum was measured using a UV-vis spectrophotometer (peak absorption at λ = 540 nm). The NO_2^- concentration–absorbance standard curve was made using a series of standard KNO_2 solutions (see Fig. S13).

Determination of NO_3^-

The concentration of NO_3^- was determined by spectrophotometry. A specific volume of electrolyte was extracted from the electrolytic cell and diluted to fall within the detection range. Subsequently, 0.1 mL of 1 M HCl solution and 10 μL of 0.8% sulfamic acid solution were added to 5 mL of the above solution, followed by thorough mixing. The absorption spectrum was measured using a UV-vis spectrometer, and the absorption intensities at both wavelengths of 220 and 275 nm were recorded. The final absorbance was obtained according to $A = A_{220\ nm} - A_{275\ nm}$. The concentration-absorbance standard curve was made using a series of standard KNO_3 solutions (see Fig. S14).

^1H NMR determination of NH_3

$K^{15}NO_3$ was used as the feeding N-source to conduct the isotopically labelled nitrate reduction experiments. After electrochemical reduction of $^{15}NO_3^-$, 0.2 mL of the electrolyte with $^{15}NH_3$ produced was extracted and the pH was adjusted to approximately 3 using a 0.05 M H_2SO_4 solution, resulting in a final volume of 0.4 mL. Then 0.1 mL of maleic acid solution (0.4 mg mL^{-1}) and 50 μL of deuterium oxide (D_2O) were added to this diluted solution for ^1H NMR quantification. The NH_3 concentrations were determined by the peak area ratios between $^{15}NH_4^+$ and maleic acid. A series of $^{15}NH_4Cl$ solutions of different concentrations containing maleic acid were prepared as standard solutions to get the standard calibration curve. $^{14}NH_4^+$ was determined using the same method, but with $K^{14}NO_3$ as the feeding N-source (see Figs. S23 and S24).

^1H NMR determination of formate, FDCA and INA

The identification and quantification of formate, FDCA and INA were conducted using ^1H NMR, employing calibration curves with DMSO solution (1 mg mL^{-1}) as an internal standard. For ^1H NMR determination, 400 μL of electrolyte from anolyte post electrolysis were added into 100 μL of DMSO and 50 μL D_2O. A series of solutions of their targeted formate derivatives with known concentrations were prepared for acquiring the corresponding standard calibration curves (see Figs. S46, S52 and S53).

Calculations of Faradaic efficiency (FE), yield, yield rate, conversion rate, energy efficiency and collection efficiency

The FEs of electrocatalytic NO_3^- to NH_3 conversion and NO_3^- to NO_2^- conversion were calculated as follows:

$$FE_{NH_3} = (8 \times F \times C_{NH_3} \times V)/(17 \times Q) \times 100\% \quad \text{(Eq. 1)}$$

$$FE_{NO_2^-} = (2 \times F \times C_{NO_2^-} \times V)/(46 \times Q) \times 100\% \quad \text{(Eq. 2)}$$

The NH_3 yield rate (mg $h^{-1}cm^{-2}$) was calculated using the following equation:

$$r_{NH_3} = (C_{NH_3} \times V)/(t \times S) \quad \text{(Eq. 3)}$$

The conversion rates of NO_3^- and HCHO were calculated as follows:

$$\text{Conversion rate} = n[\text{mole}]_{\text{consumed}}/n[\text{mole}]_{\text{initial}} \times 100\% \quad \text{(Eq. 4)}$$

The H_2 gas production was collected by the downward drainage method. The actually produced H_2 amount was calculated as follows:

$$n[\text{mole}]_{\text{actually produced}} = V_{H_2}/22.4 \quad \text{(Eq. 5)}$$

The theoretically produced H_2 amount was calculated as follows:

$$n[\text{mole}]_{\text{theoretically produced}} = Q/(n \times F) \quad \text{(Eq. 6)}$$

The FEs of formate, FDCA, INA were calculated as follows:

$$FE_{\text{acid}} = (n[\text{mole}]_{\text{acid}} \times n \times F)/Q \times 100\% \quad \text{(Eq. 7)}$$

The yield rates of formate, FDCA, INA were calculated as follows:

$$r_{\text{acid}} = (C_{\text{acid}} \times V)/(t \times S) \quad \text{(Eq. 8)}$$

The energy efficiency (EE) was defined as the ratio of fuel energy to applied electrical power, which was calculated as follows:

$$EE_{NH_3} = \frac{\left|E^{\theta}_{FOR} - E^{\theta}_{NH_3}\right|}{E_{cell}} \times FE_{NH_3} \times 100\% \quad \text{(Eq. 9)}$$

The yields of formate, INA and FDCA were calculated as follows:

$$\text{Yield}_{\text{acid}} = (n[\text{mole}]_{\text{acid formed}}/n[\text{mole}]_{\text{aldehyde initial}}) \times 100\% \quad \text{(Eq. 10)}$$

The collection efficiency of $HCOONH_4$, ammonium furandicarboxylic acid and ammonium isonicotinic acid were calculated as follows:

$$R = n[\text{mole}]_{\text{collected}}/n[\text{mole}]_{\text{theoretically produced}} \quad \text{(Eq. 11)}$$

where F is the Faraday constant (96,485 C mol^{-1}), C_{NH3} is the measured NH_3 concentration, C_{acid} is the measured acid concentration, V is the volume of the electrolyte, Q is the total charge passing the electrode, t is the reduction time, S is the geometric area of the working electrode, V_{H2} is the volume of H_2 gas collected, n[mole] is the mole number of the substrate, n is the number of electrons transferred for each product molecule, E^{θ}_{NH3} represents the thermodynamic equilibrium potential of NO_3^- electroreduction to NH_3 (0.69 V vs. RHE), E^{θ}_{FOR} is the thermodynamic equilibrium potential of the FOR (−0.22 V vs. RHE), E_{cell} is the applied cell voltage.

Computing details

All spin-polarized density functional theory (DFT) calculations were implemented within the Vienna ab initio Simulation Package (VASP). The Perdew-Burke-Ernzerhof (PBE) functional and the generalized gradient approximation (GGA) approach was used to described electron exchange correlation potential, the projector-augmented-wave (PAW) pseudopotential was applied to treat the ion-electron interactions, a plane-wave cutoff energy was set to 600 eV and with a 5 × 5 × 1 Monkhorst-Pack k-point mesh was applied to sample the Brillouin zone in the electronic and ionic optimization, until an energy convergence of 10^{-5} eV/atom and a force convergence of -0.02 eV $Å^{-1}$ for each atom under the conjugate gradient (CG) algorithm, respectively. To consider the van der Waals interactions between the substrate and adsorbents, Grimme's semiempirical DFT-D3 approach was used to correct Gibbs free energy. Furthermore, to avoid the interactions between different interlayer which was produced from the periodic boundary condition, a 20 Å vacuum space was set along the *Z* direction. The free energy changes (ΔG) of intermediate species during NO_3^-RR were calculated using the following equation:

$$\Delta G = \Delta E + \Delta E_{ZPE} - T\Delta S \tag{Eq. 12}$$

where ΔE is the binding energy, ΔE_{ZPE} and ΔS are the difference in zero-point energy and entropy change, respectively, and T is the temperature. ΔG of each elementary reaction step of NO_3^-RR on Cu-based catalysts were simulated according to the following reactions (* represents the adsorption site.):

$$NO_3^- + * \rightarrow *NO_3 + e^- \tag{Eq. 13}$$

$$*NO_3 + H_2O + 2e^- \rightarrow *NO_2 + 2OH^- \tag{Eq. 14}$$

$$*NO_2 + H_2O + 2e^- \rightarrow *NO + 2OH^- \tag{Eq. 15}$$

$$*NO + H_2O + e^- \rightarrow *NHO + OH^- \tag{Eq. 16}$$

$$*NHO + H_2O + e^- \rightarrow *NH_2O + OH^- \tag{Eq. 17}$$

$$*NH_2O + H_2O + e^- \rightarrow *NH_2OH + OH^- \tag{Eq. 18}$$

$$*NH_2OH + e^- \rightarrow *NH_2 + OH^- \tag{Eq. 19}$$

$$*NH_2 + H_2O + e^- \rightarrow *NH_3 + OH^- \tag{Eq. 20}$$

$$*NH_3 \rightarrow NH_3 + * \tag{Eq. 21}$$

Supplementary Figures

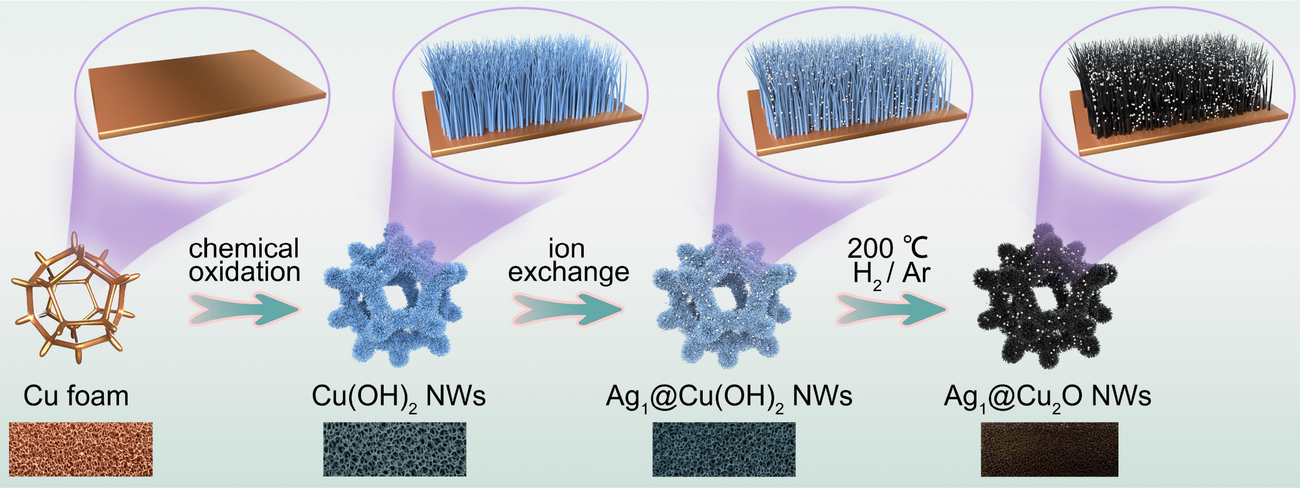

Fig. S1 Schematic synthesis of $Ag_1@Cu_2O$ NWs catalyst.

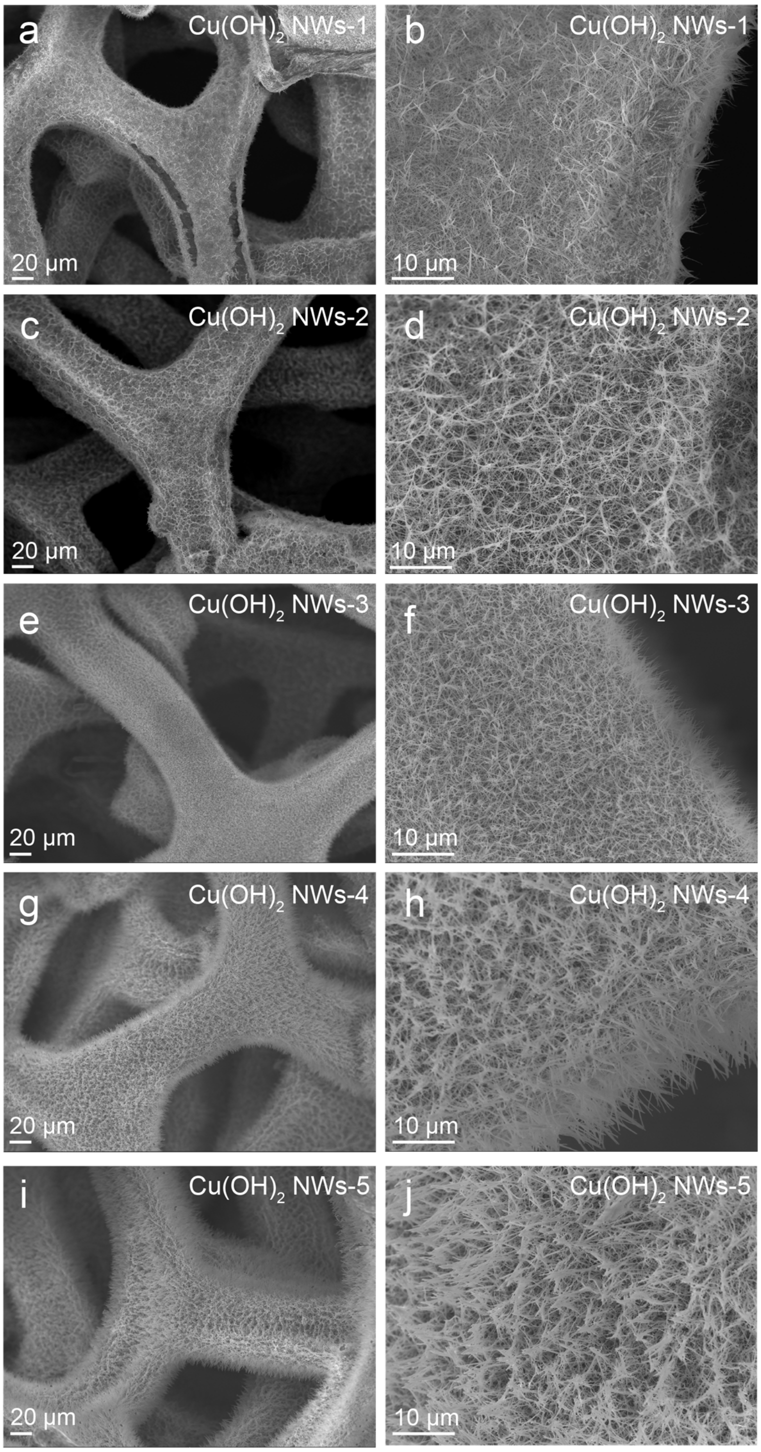

Fig. S2 SEM images of $Cu(OH)_2$ NWs obtained at different growth times. (a, b) $Cu(OH)_2$ NWs-1; (c, d) $Cu(OH)_2$ NWs-2; (e, f) $Cu(OH)_2$ NWs-3; (g, h) $Cu(OH)_2$ NWs-4; and (i, j) $Cu(OH)_2$ NWs-5. As clearly observed in these SEM images, after 40 min of growth, the surface of Cu foam exhibited a highly dense array of nanowires, thereby facilitating an enhanced carrier capacity for subsequent loading of Ag single-atom sites.

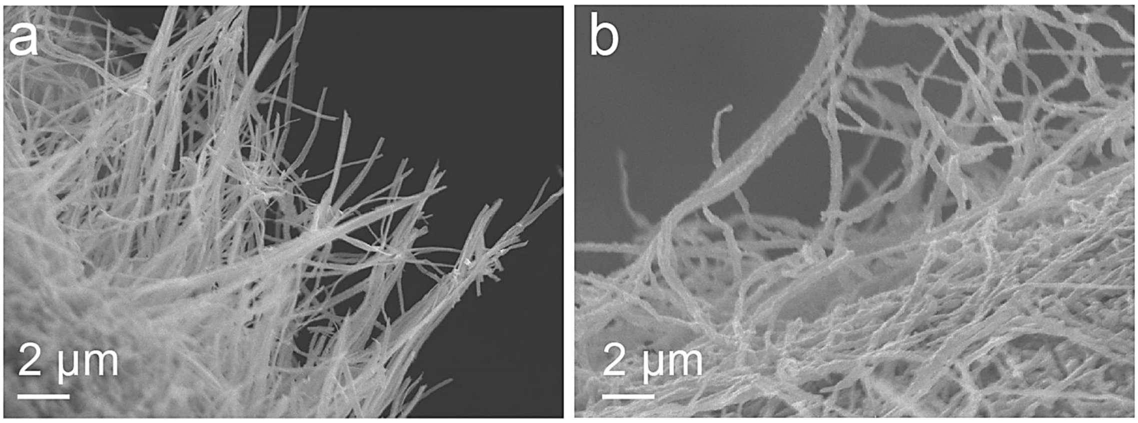

Fig. S3 SEM images of (a) Cu_2O NWs and (b) $Ag_1@Cu_2O$ NWs.

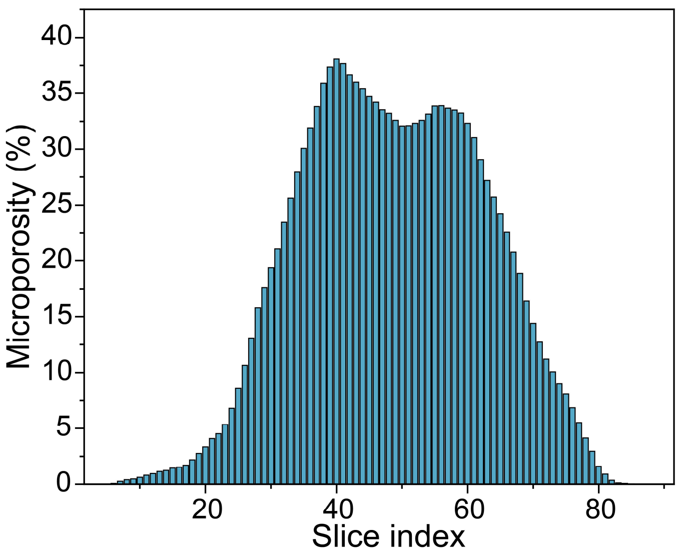

Fig. S4 The microporosity of the layer-by-layer slices after 3D reconstruction of a single $Ag_1@Cu_2O$ nanowire.

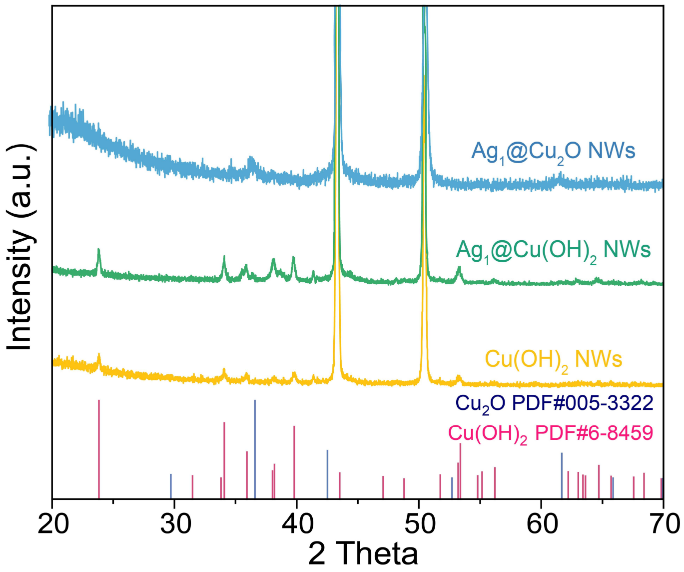

Fig. S5 XRD patterns of $Cu(OH)_2$ NWs, $Ag_1@Cu(OH)_2$ NWs and $Ag_1@Cu_2O$ NWs.

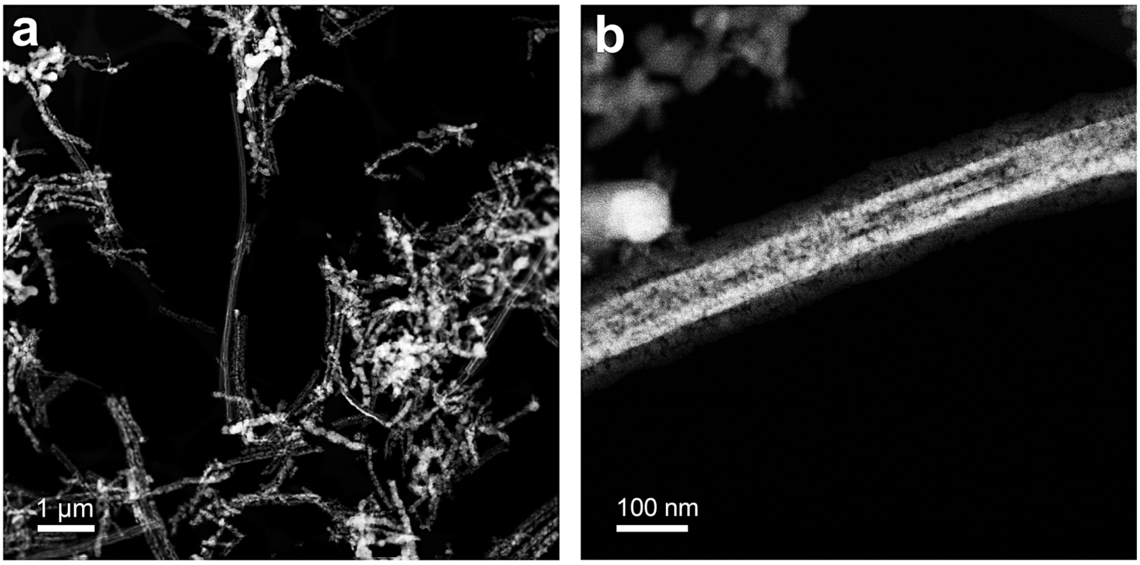

Fig. S6 HAADF-TEM images of $Ag_1@Cu_2O$ NWs at (a) low and (b) high magnifications.

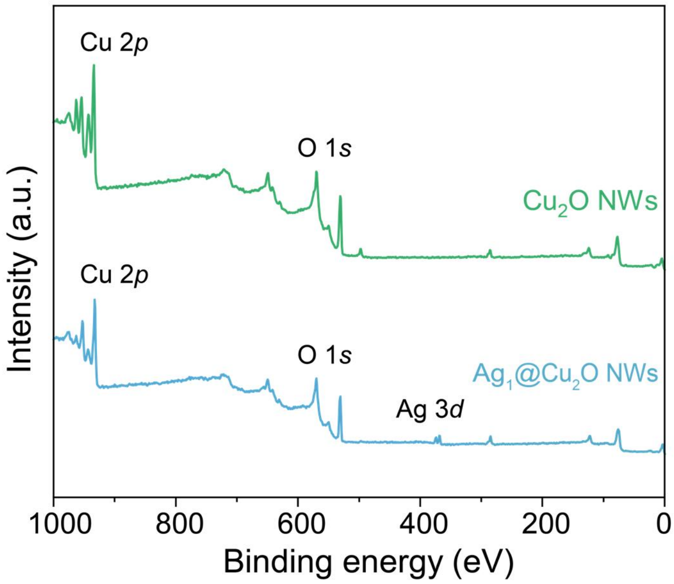

Fig. S7 Survey XPS spectra of Cu_2O NWs and $Ag_1@Cu_2O$ NWs. The XPS survey spectra confirmed the presence of Ag, Cu and O elements exclusively in $Ag_1@Cu_2O$ NWs.

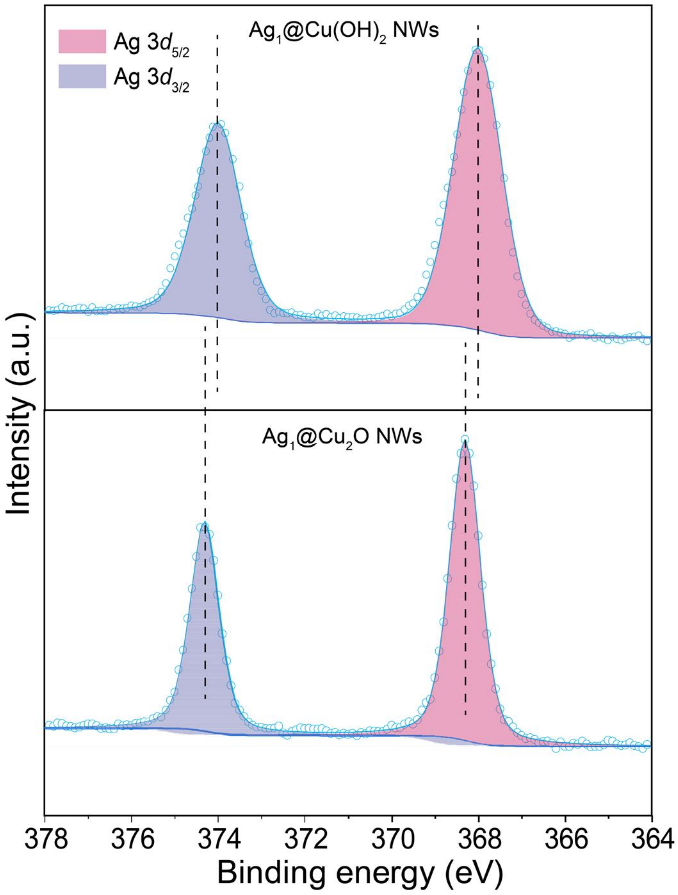

Fig. S8 High-resolution Ag 3*d* XPS spectra of $Ag_1@Cu(OH)_2$ NWs and $Ag_1@Cu_2O$ NWs. In the high-resolution Ag 3*d* spectra, the binding energies of Ag $3d_{5/2}$ (368.3 eV) and Ag $3d_{3/2}$ (374.3 eV) for $Ag_1@Cu_2O$ exhibit a slight upshift compared to those of $Ag_1@Cu(OH)_2$ NWs, indicating the Ag single-atoms carry a partial positive charge due to electron transfer from Ag to Cu.[1]

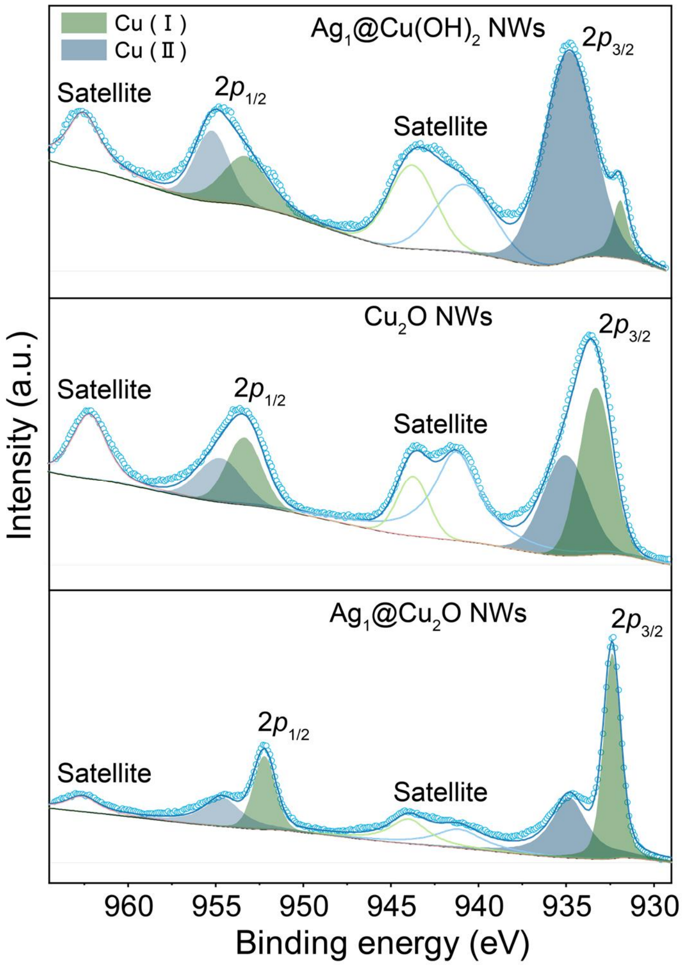

Fig. S9 High-resolution Cu 2*p* XPS spectra of Ag$_1$@Cu(OH)$_2$ NWs, Cu$_2$O NWs and Ag$_1$@Cu$_2$O NWs. In the high-resolution Cu 2*p* spectrum, Ag$_1$@Cu(OH)$_2$ NWs predominantly exhibit typical features of Cu^{2+} species. Following treatment with H$_2$/Ar, the spectrum of Ag$_1$@Cu$_2$O NWs is dominated by Cu^0/Cu^{1+} species, suggesting the reduction of surface Cu^{2+}, and residual Cu^{2+} peaks may be attributed to inadvertent oxidation from air exposure. A notable downshift of 0.8 eV in the Cu^0/Cu^{1+} binding energies was observed when comparing Ag$_1$@Cu$_2$O NWs (933.2 and 953.1 eV) with Cu$_2$O NWs (932.4 and 952.3 eV), indicating partial interfacial electron transfer from Ag single-atoms to the Cu$_2$O NWs support.[2,3]

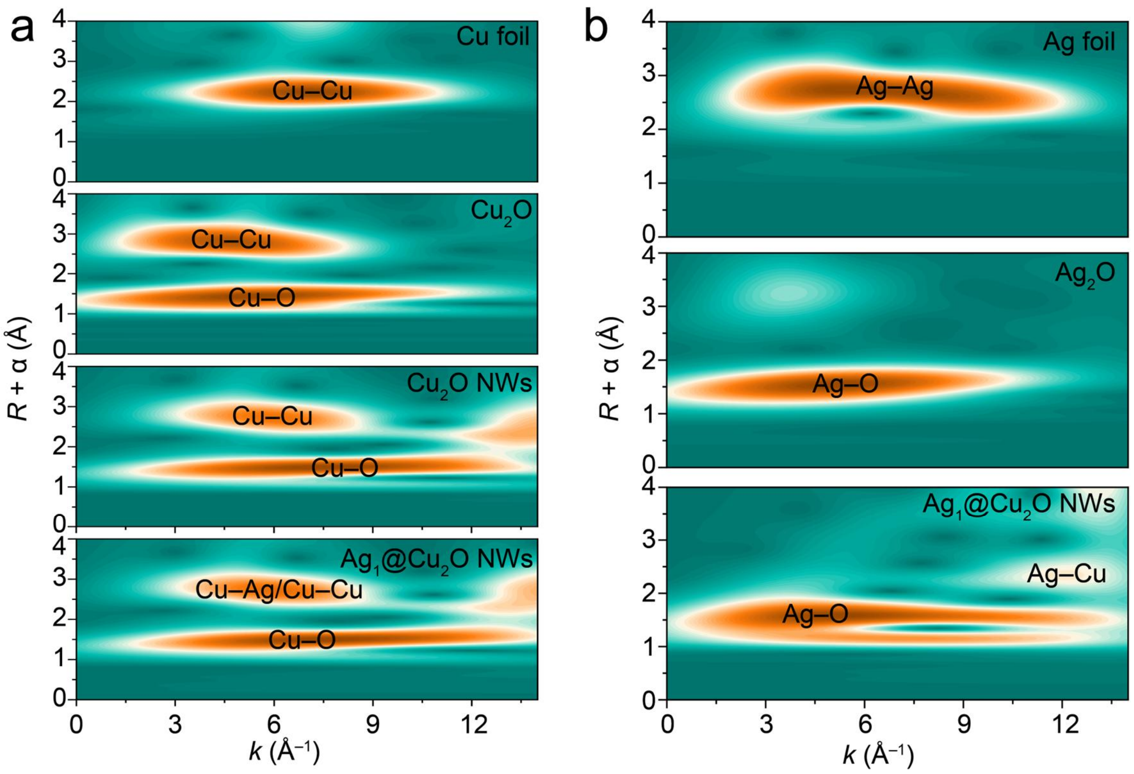

Fig. S10 Wavelet transform (WT) k^2-weighted EXAFS spectra analysis. (a) Cu foil, Cu_2O, Cu_2O NWs and $Ag_1@Cu_2O$ NWs; (b) Ag foil, Ag_2O and $Ag_1@Cu_2O$ NWs. The WT maximum at 8.2 Å^{-1} and 6.2 Å^{-1} for $Ag_1@Cu_2O$ NWs are attributed to the Cu−O and Cu−Ag/Cu−Cu bonds, respectively, which are consistent with the EXAFS results. Similarly, the WT maximum at 4.9 Å^{-1} and 12.2 Å^{-1} for $Ag_1@Cu_2O$ NWs are attributed to the Ag−O and Ag−Cu bonds, respectively. The above results depict the Ag single-atom coordination structure in $Ag_1@Cu_2O$ NWs.

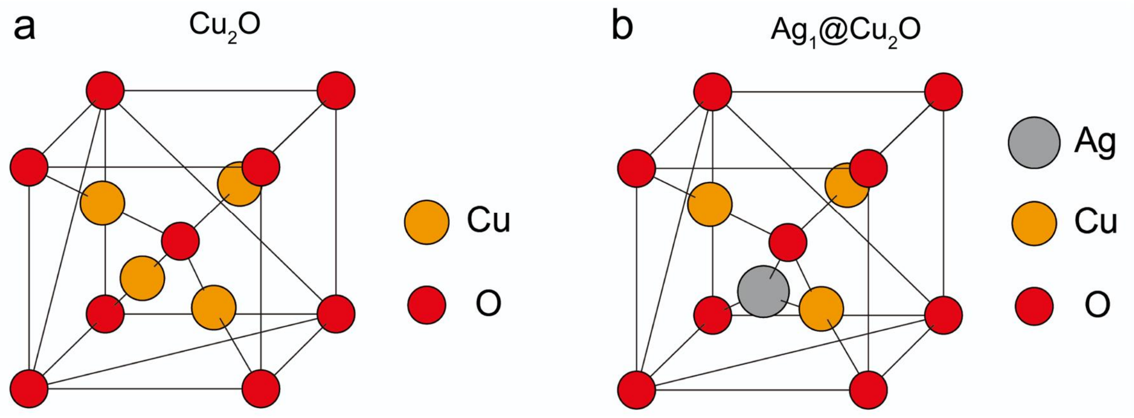

Fig. S11 Proposed local coordination structures of (a) Cu_2O and (b) $Ag_1@Cu_2O$.

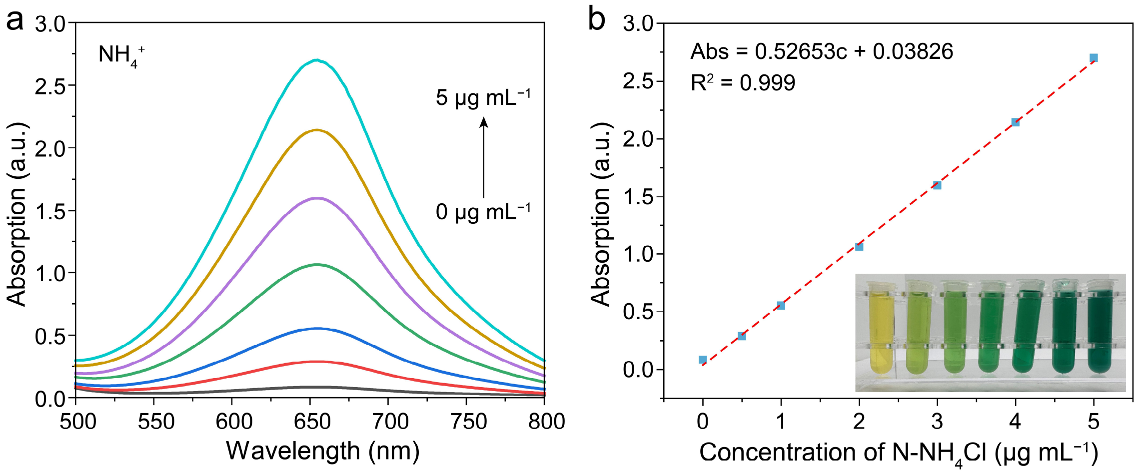

Fig. S12 NH_3 quantification using UV-vis absorption spectroscopy. (a) UV-vis absorption spectra; (b) corresponding standard calibration curve for NH_3 assay using the indophenol blue method.

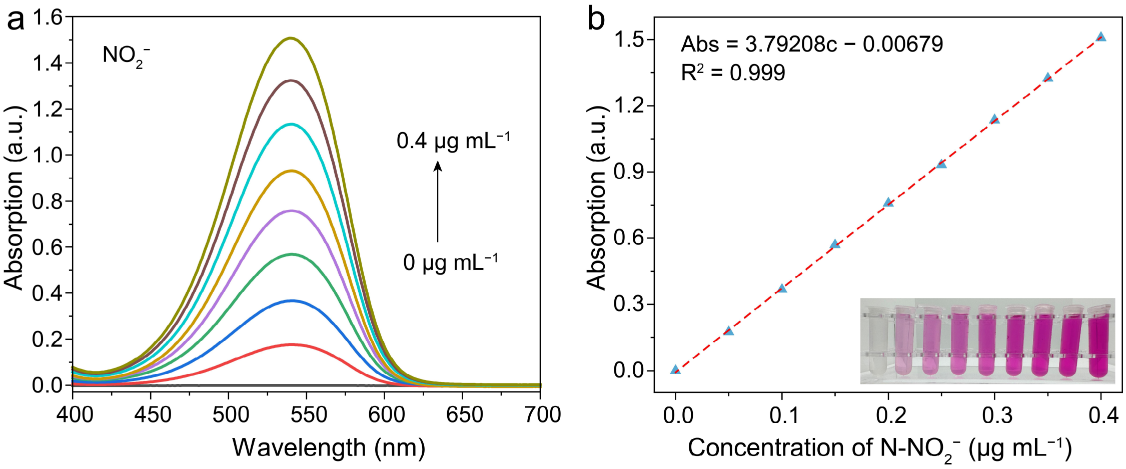

Fig. S13 NO_2^- quantification using UV-vis absorption spectroscopy. (a) UV-vis absorption spectra; (b) corresponding standard calibration curve for NO_2^- assay using the indophenol blue method.

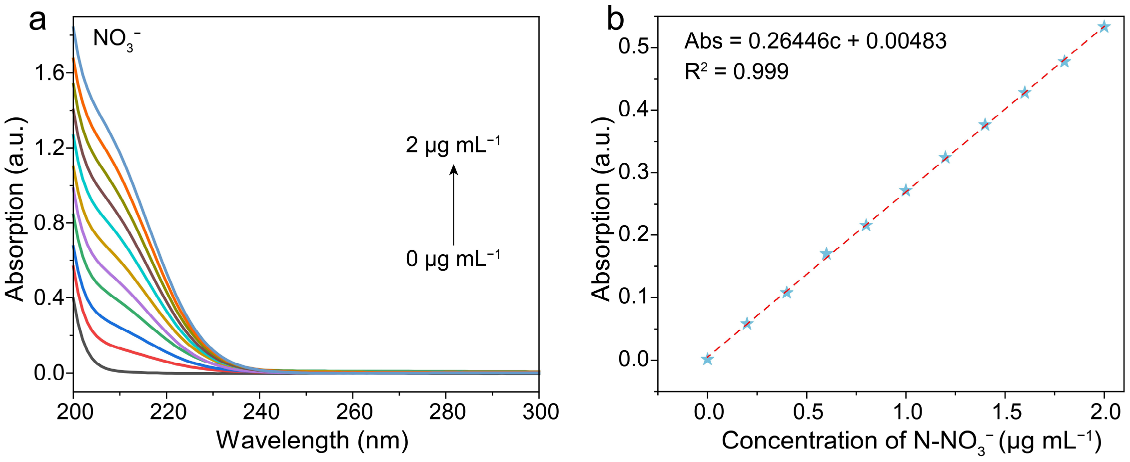

Fig. S14 NO$_3^-$ quantification using UV-vis absorption spectroscopy. (a) UV-vis absorption spectra; (b) corresponding standard calibration curve for NO$_3^-$ assay using the indophenol blue method.

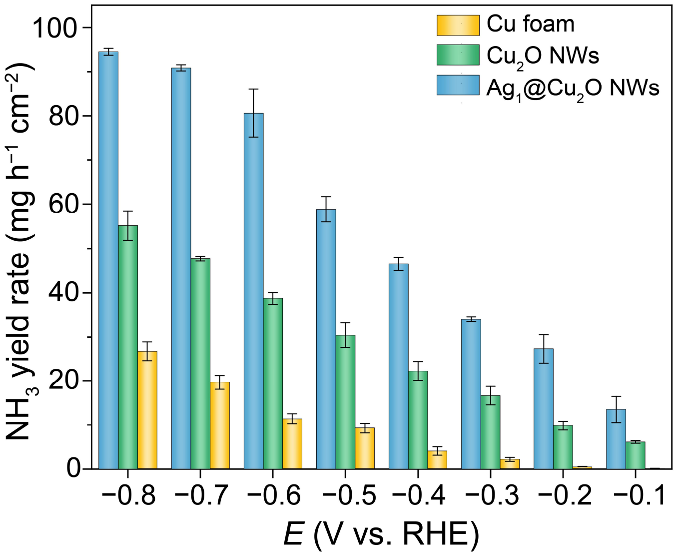

Fig. S15 NH_3 yield rates on Cu foam, Cu_2O NWs and $Ag_1@Cu_2O$ NWs in 1 M KOH with 250 mM NO_3^- over a potential range of −0.1 to −0.8 V vs. RHE. Error bars represent the standard deviation of at least three independent measurements, with the center value being their average.

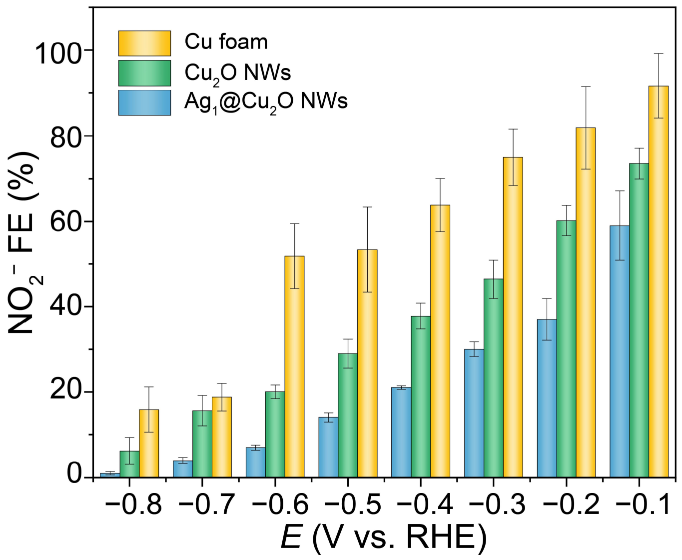

Fig. S16 FEs of NO_3^--to-NO_2^- conversion on Cu foam, Cu_2O NWs and $Ag_1@Cu_2O$ NWs in 1 M KOH with 250 mM NO_3^- over a potential range of −0.1 to −0.8 V vs. RHE. Error bars represent the standard deviation of at least three independent measurements, with the center value being their average.

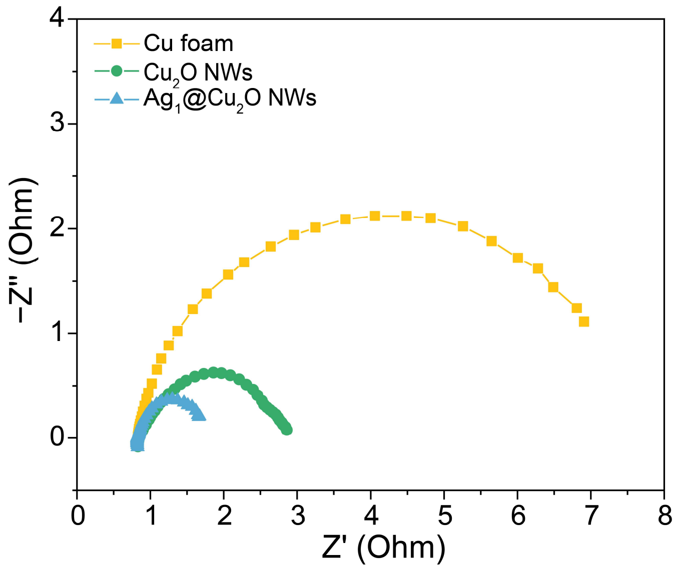

Fig. S17 Electrochemical impedance spectra (Nyquist plots) of Cu foam, Cu_2O NWs and $Ag_1@Cu_2O$ NWs.

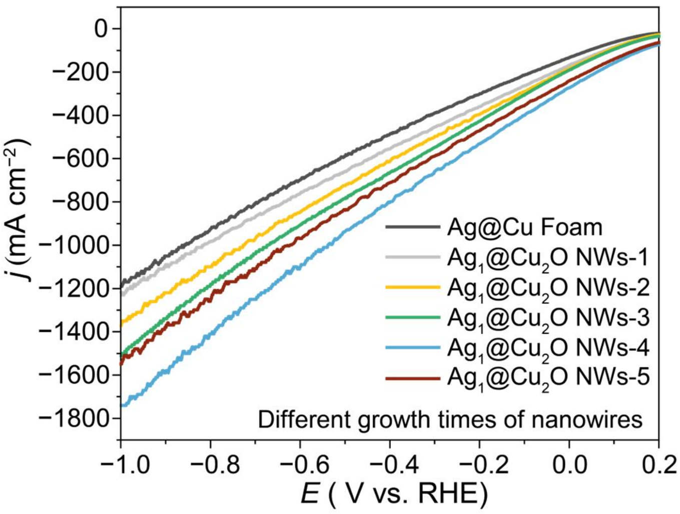

Fig. S18 LSV curves of Ag_1@Cu Foam, Ag_1@Cu_2O NWs-1, Ag_1@Cu_2O NWs-2, Ag_1@Cu_2O NWs-3, Ag_1@Cu_2O NWs-4 and Ag_1@Cu_2O NWs-5 in a 1 M KOH with 250 mM NO_3^- electrolyte. Note: The samples were obtained using a similar methodology as that of Ag_1@Cu_2O NWs, albeit with varying growth time during the process.

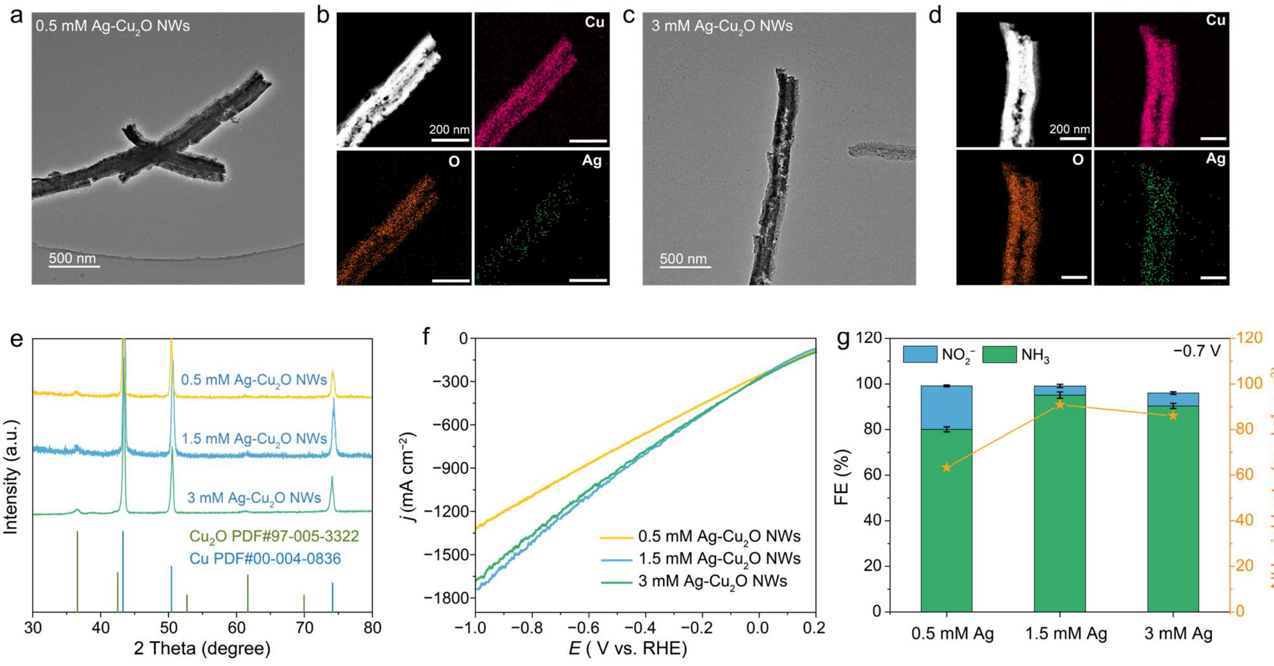

Fig. S19 (a) TEM image and (b) EDS mappings of 0.5 mM Ag-Cu$_2$O NWs. (c) TEM image and (d) EDS mappings of 3 mM Ag-Cu$_2$O NWs. (e) XRD patterns of 0.5 mM Ag-Cu$_2$O NWs, 1.5 mM Ag-Cu$_2$O NWs and 3 mM Ag-Cu$_2$O NWs. (f) LSV curves of 0.5 mM Ag-Cu$_2$O NWs, 1.5 mM Ag-Cu$_2$O NWs and 3 mM Ag-Cu$_2$O NWs in a 1 M KOH with 250 mM NO_3^- electrolyte. (g) NH_3 FEs, NO_3^--to-NO_2^- FEs and NH_3 yield rates on of 0.5 mM Ag-Cu$_2$O NWs, 1.5 mM Ag-Cu$_2$O NWs and 3 mM Ag-Cu$_2$O NWs at −0.7 V vs. RHE. Note: The samples were obtained using a similar methodology as that of Ag$_1$@Cu$_2$O NWs, albeit with varying amounts of Ag$^+$ introduced during the process.

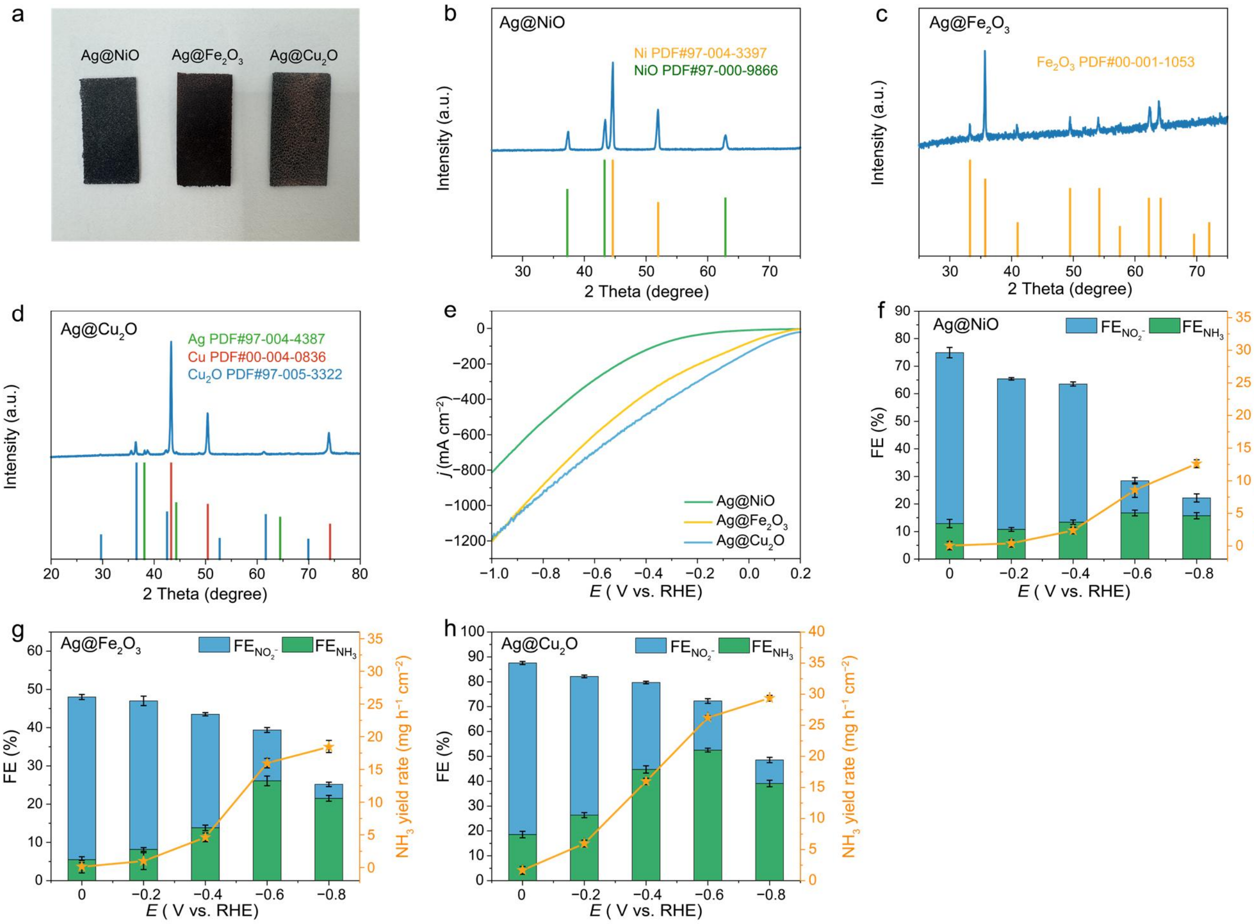

Fig. S20 Electrocatalytic NO_3^-RR performances of samples in 1 M KOH with 250 mM NO_3^-. (a) Photographs of Ag@NiO/Ni foam, Ag@Fe_2O_3/Fe foam and Ag@Cu_2O/Cu foam. XRD patterns of (b) Ag@NiO/Ni foam, (c) Ag@Fe_2O_3/Fe foam and (d) Ag@Cu_2O/Cu foam. (e) LSV curves of Ag@NiO/Ni foam, Ag@Fe_2O_3/Fe foam and Ag@Cu_2O/Cu foam. NH_3 FEs, NO_3^--to-NO_2^- FEs and NH_3 yield rates on (f) Ag@NiO/Ni foam, (g) Ag@Fe_2O_3/Fe foam and (h) Ag@Cu_2O/Cu foam. Note: The samples were obtained with the direct use of metal foam for Ag growth through a similar ion exchange as that for Ag_1@Cu_2O NWs synthesis.

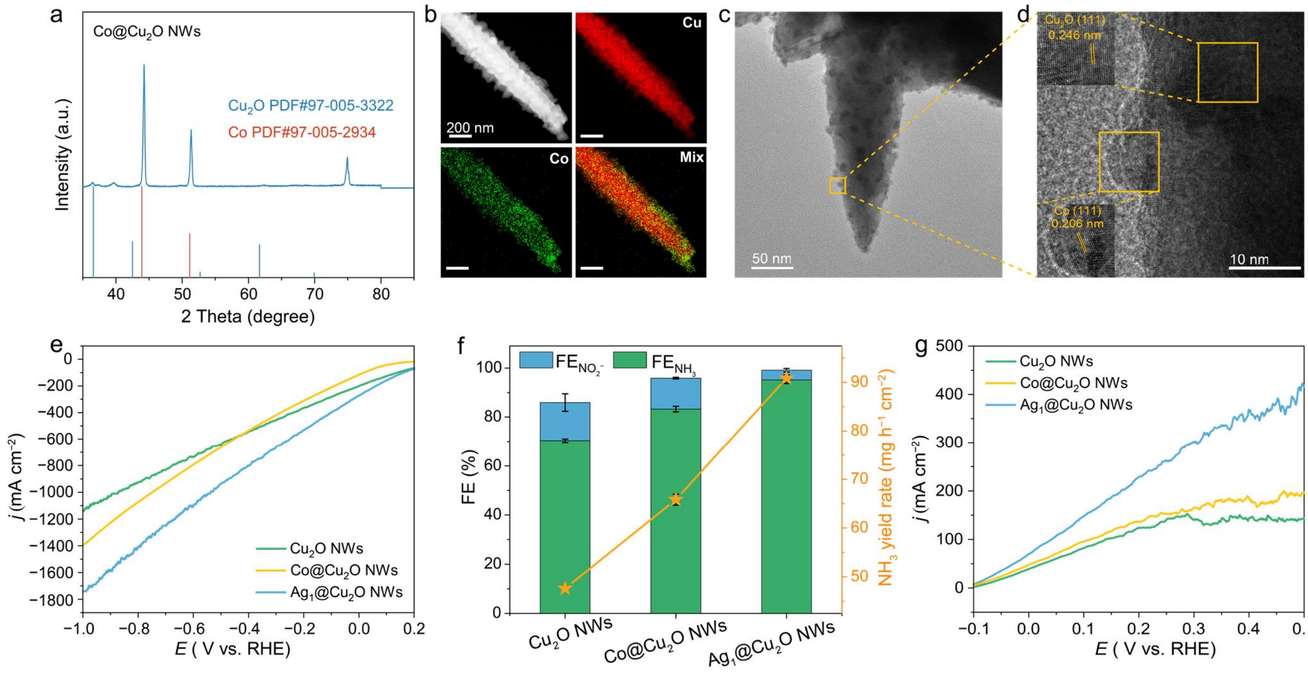

Fig. S21 (a) XRD pattern, (b) EDS mappings, (c, d) TEM images of Co@Cu$_2$O NWs. (e) LSV curves of Cu$_2$O NWs, Co@Cu$_2$O NWs and Ag$_1$Cu$_2$O NWs in a 1 M KOH with 250 mM NO$_3^-$ electrolyte. (f) NH$_3$ FEs, NO$_3^-$-to-NO$_2^-$ FEs and NH$_3$ yield rates on Cu$_2$O NWs, Co@Cu$_2$O NWs and Ag$_1$@Cu$_2$O NWs at −0.7 V vs. RHE. (g) LSV curves of Cu$_2$O NWs, Co@Cu$_2$O NWs and Ag$_1$@Cu$_2$O NWs in a 1 M KOH with 0.2 M HCHO electrolyte. Note: The Co@Cu$_2$O NWs sample was obtained using an electrodeposition methodology with Cu$_2$O NWs as the working electrode in a 1 M KOH electrolyte containing 0.1 M CoSO$_4$ at −1 V vs. Ag/AgCl for 1200 s.

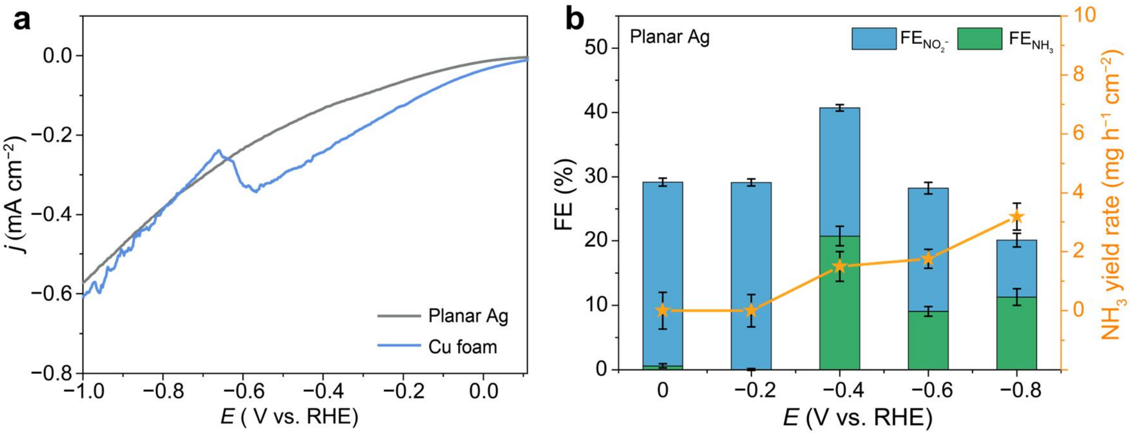

Fig. S22 (a) LSV curves of planar Ag and Cu foam in a 1 M KOH with 250 mM NO_3^- electrolyte. (b) NH_3 FEs and yield rates on planar Ag. Error bars represent the standard deviation of at least three independent measurements, with the center value being their average. Note: The planar Ag is a commercial Ag foil with an area of 1 × 1 cm^2.

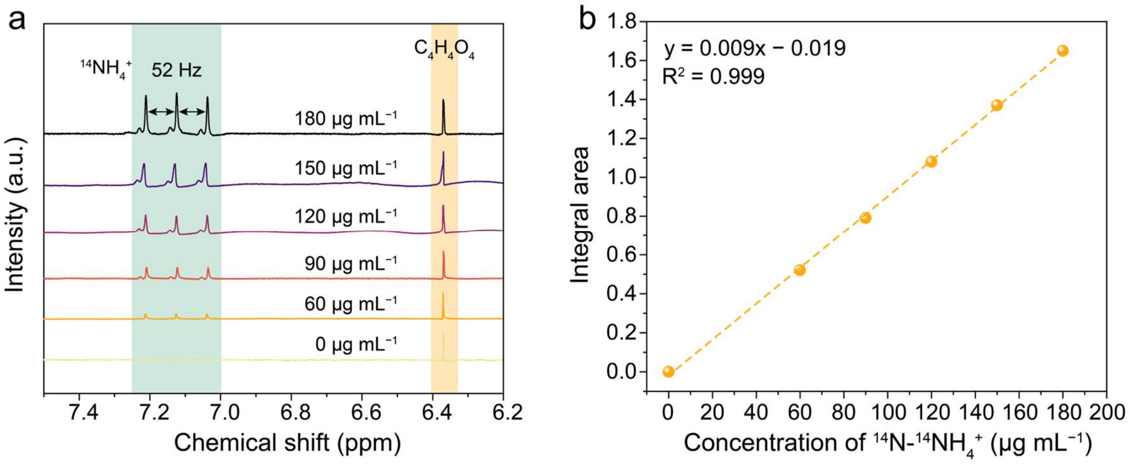

Fig. S23 Standard calibration curve for $^{14}NH_4^+$ quantification by ^1H NMR. (a) ^1H NMR spectra of ammonia-^{14}N at different concentrations; (b) the corresponding standard calibration curve. The concentration of $^{14}NH_4^+$ can be quantitatively determined by ^1H NMR with maleic acid as an external standard.

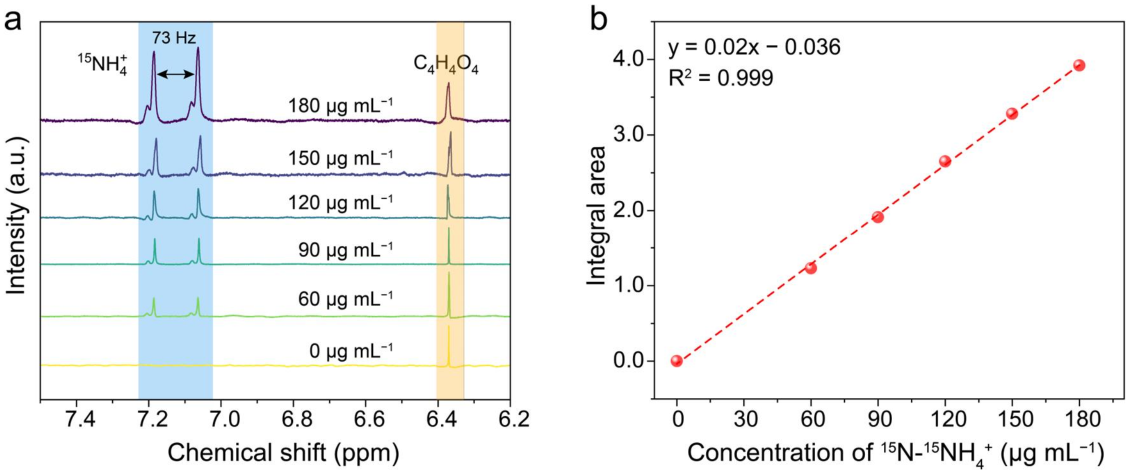

Fig. S24 Standard calibration curve for $^{15}NH_4^+$ quantification by ^1H NMR. (a) ^1H NMR spectra of ammonia-^{15}N at different concentrations; (b) the corresponding standard calibration curve. The concentration of $^{15}NH_4^+$ can be quantitatively determined by ^1H NMR with maleic acid as an external standard.

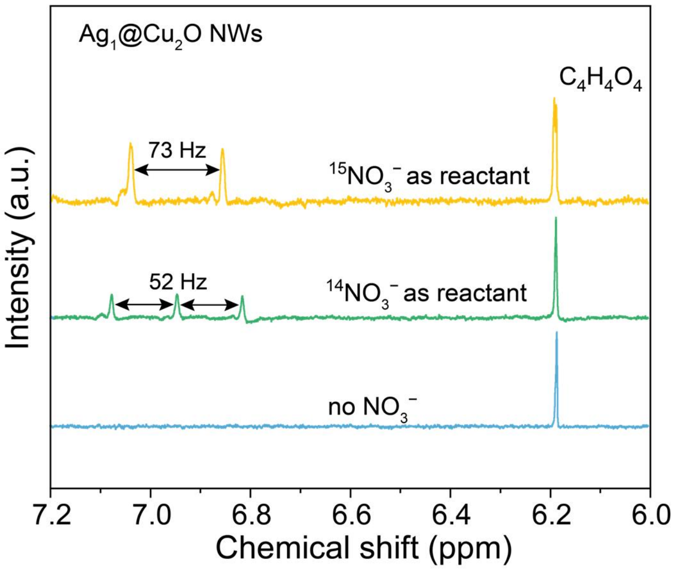

Fig. S25 ^{1}H NMR spectra of the electrolyte after electrocatalytic NO_3^-RR on Ag_1@Cu_2O NWs at −0.7 V vs. RHE for 1 h using $^{15}NO_3^-$ and $^{14}NO_3^-$ as the N-sources, respectively. The ^{1}H NMR spectrum of $^{14}NH_3$ shows a triplet with a coupling constant of 52 Hz. When $K^{15}NO_3$ is used instead of $K^{14}NO_3$, the ^{1}H NMR spectrum of $^{15}NH_3$ product displays a distinct doublet with a coupling constant of 73 Hz.

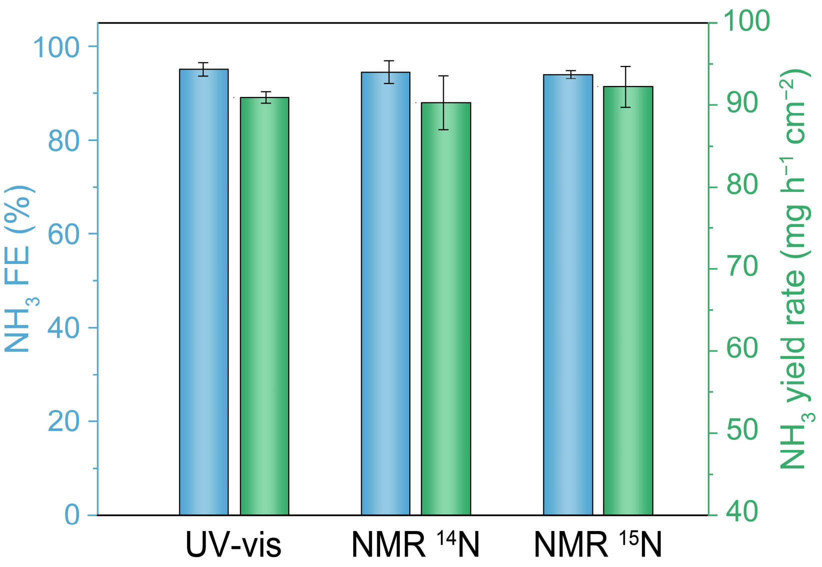

Fig. S26 Comparison of the measured NH_3 yield rate and FE over $Ag_1@Cu_2O$ NWs after electrocatalytic NO_3^-RR at −0.7 V vs. RHE based on the UV-vis and ^{1}H NMR methods, respectively, which reveals consistent results. Error bars represent the standard deviation of at least three independent measurements, with the center value being their average.

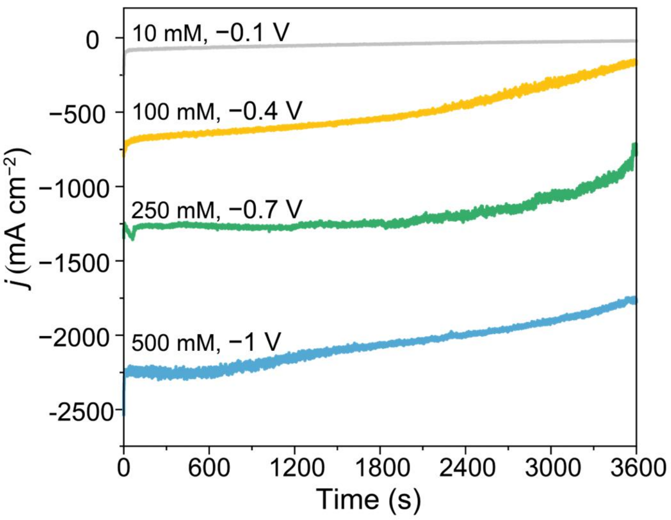

Fig. S27 *I*–*t* curves of NO_3^-RR on $Ag_1@Cu_2O$ NWs in each NO_3^- concentration at the optimal potential where the highest NH_3 yield rate was achieved, including 10 mM NO_3^- at −0.1 V vs. RHE, 100 mM NO_3^- at −0.4 V vs. RHE, 250 mM NO_3^- at −0.7 V vs. RHE and 500 mM NO_3^- at −1 V vs. RHE.

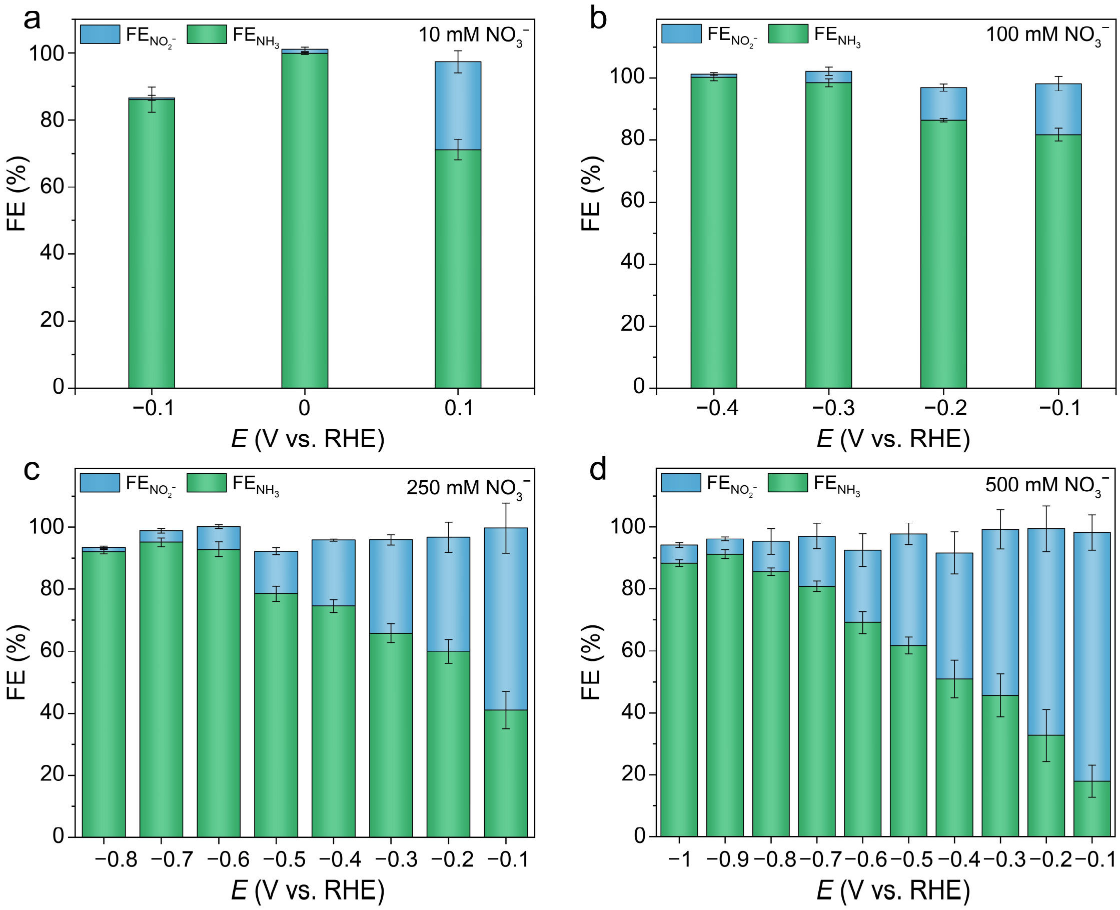

Fig. S28 Potential-dependent NH$_3$ (green bar) and NO$_2^-$ (blue bar) FEs on Ag$_1$@Cu$_2$O NWs in 1 M KOH solution with (a) 10 mM NO$_3^-$; (b) 100 mM NO$_3^-$; (c) 250 mM NO$_3^-$; and (d) 500 mM NO$_3^-$. Error bars represent the standard deviation of at least three independent measurements, with the center value being their average.

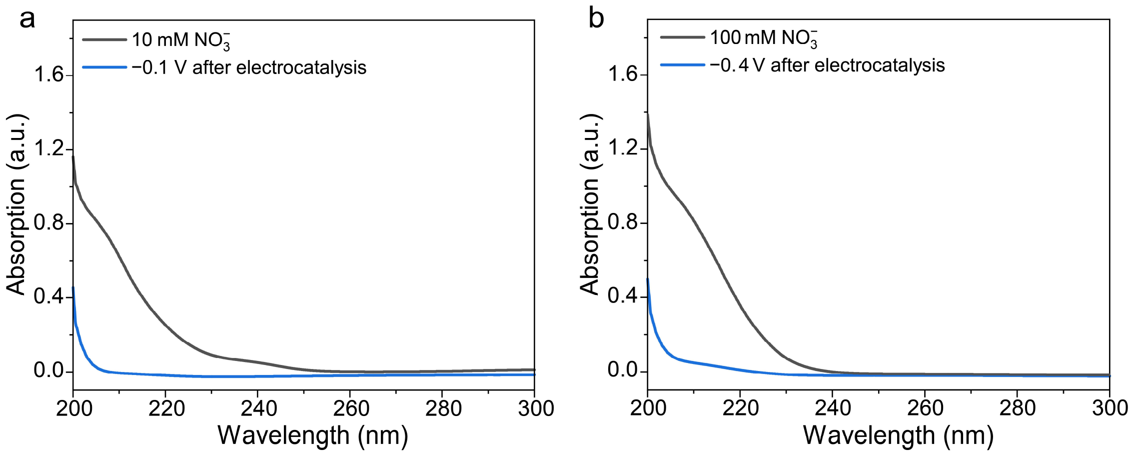

Fig. S29 UV-vis absorption spectroscopy of the electrolytes before and after NO_3^-RR on $Ag_1@Cu_2O$ NWs for 1 h. (a) 10 mM NO_3^- at −0.1 V vs. RHE. (b) 100 mM NO_3^- at −0.4 V vs. RHE.

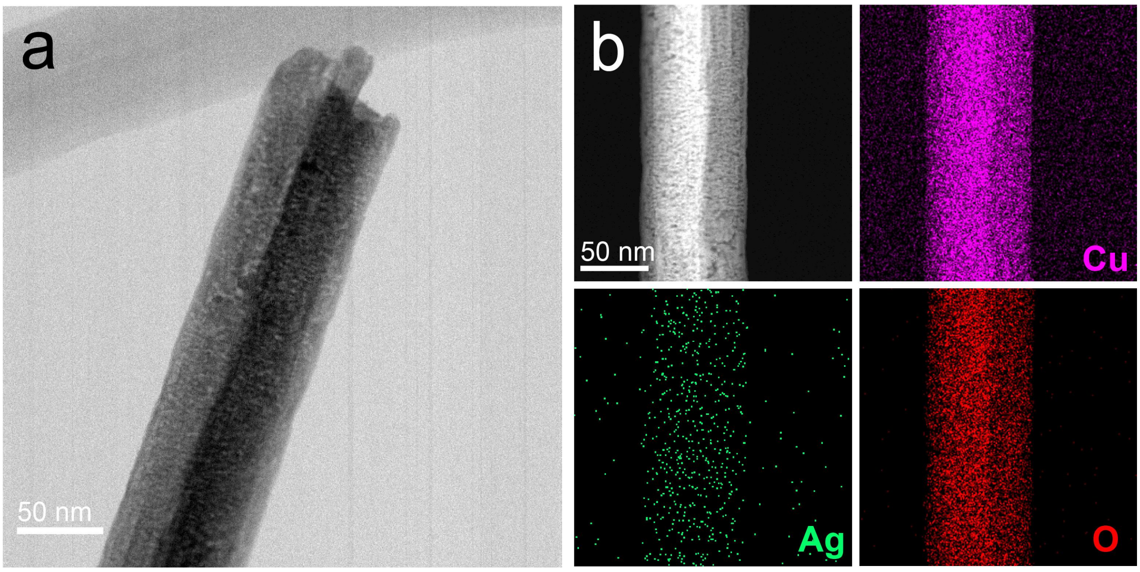

Fig. S30 (a) TEM image and (b) EDS maps of the spent $Ag_1@Cu_2O$ NWs after NO_3^-RR electrocatalytic test using CV over a potential range of −0.1 to −0.8 V vs. RHE for 30 min.

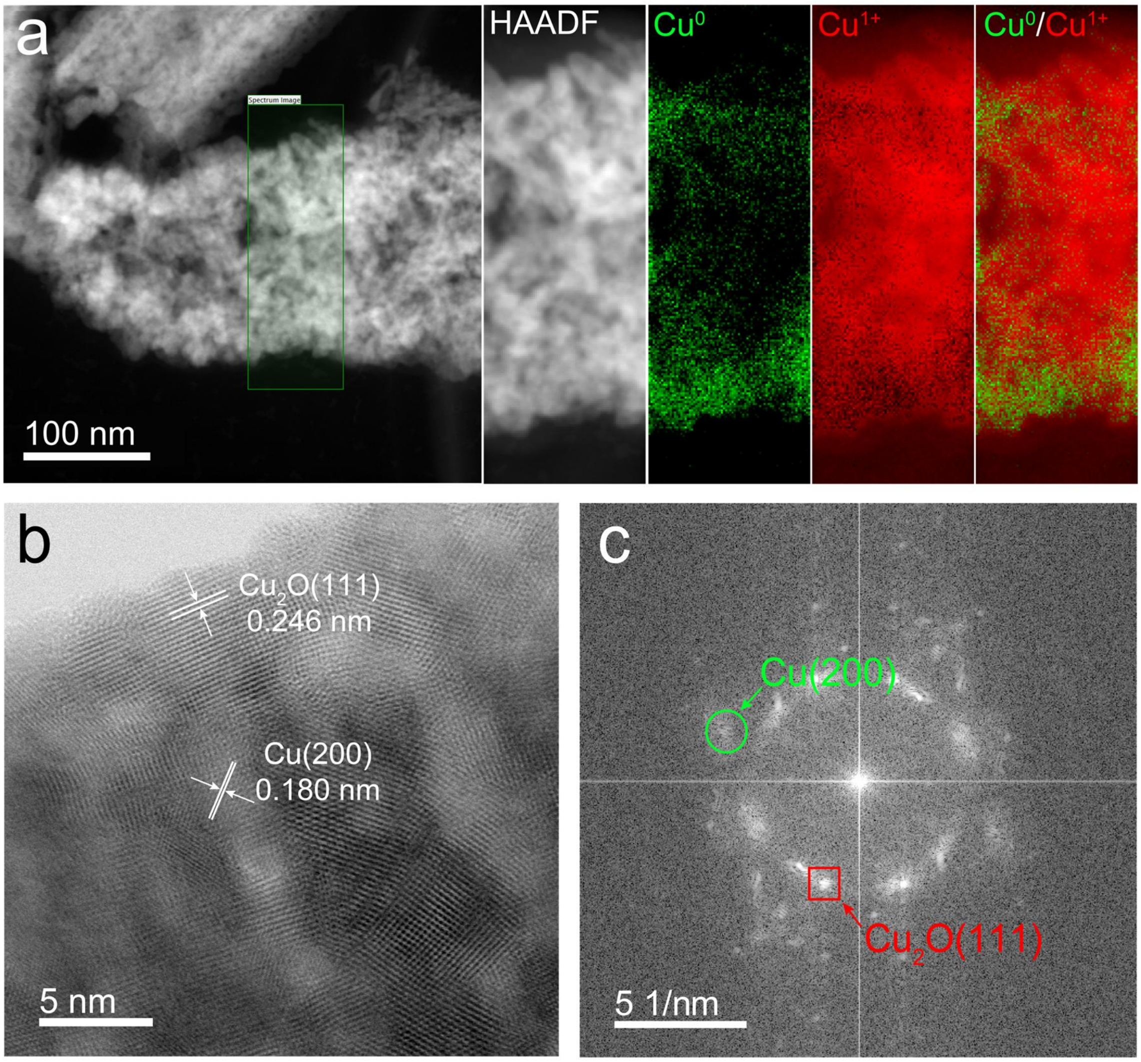

Fig. S31 TEM and EELS characterizations of the spent $Ag_1@Cu_2O$ NWs after NO_3^-RR test at –0.7 V vs. RHE for 20 h. (a) HAADF-STEM image and corresponding elemental EELS maps for Cu^0 (green) and Cu^{1+} (red). (b) HRTEM image. (c) Corresponding FFT pattern of the region shown in panel (b).

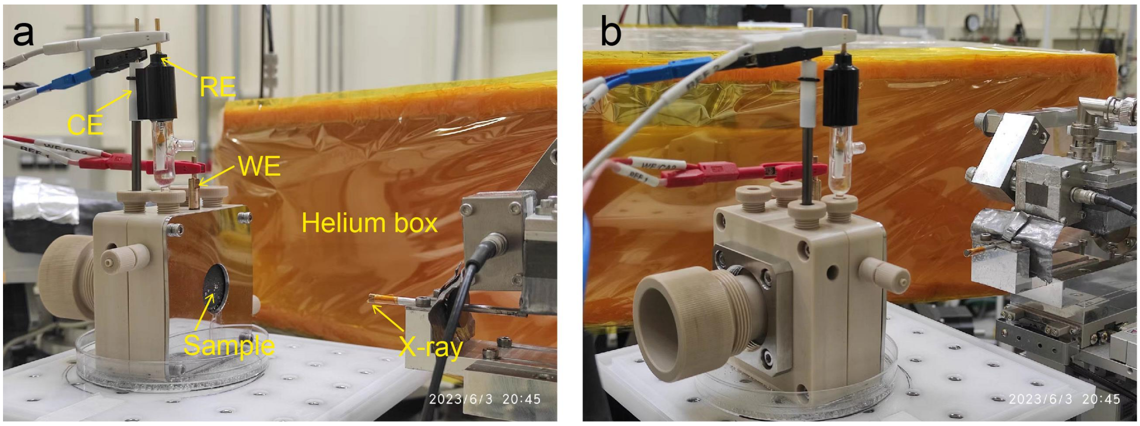

Fig. S32 Electrochemical cell used for in-situ HERFD-XAS experiment. (a) Front view and (b) back view.

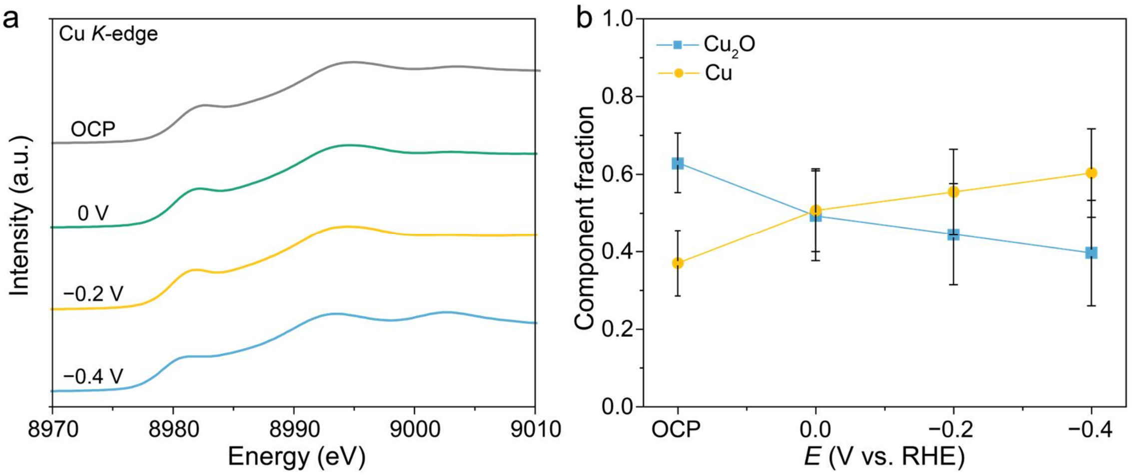

Fig. S33 (a) Linear fitting for Cu *K*-edge XANES spectra of $Ag_1@Cu_2O$ NWs at different potentials. (b) Relative fractions of Cu and Cu_2O in $Ag_1@Cu_2O$ NWs determined from the linear fitting of Cu *K*-edge XANES spectra.

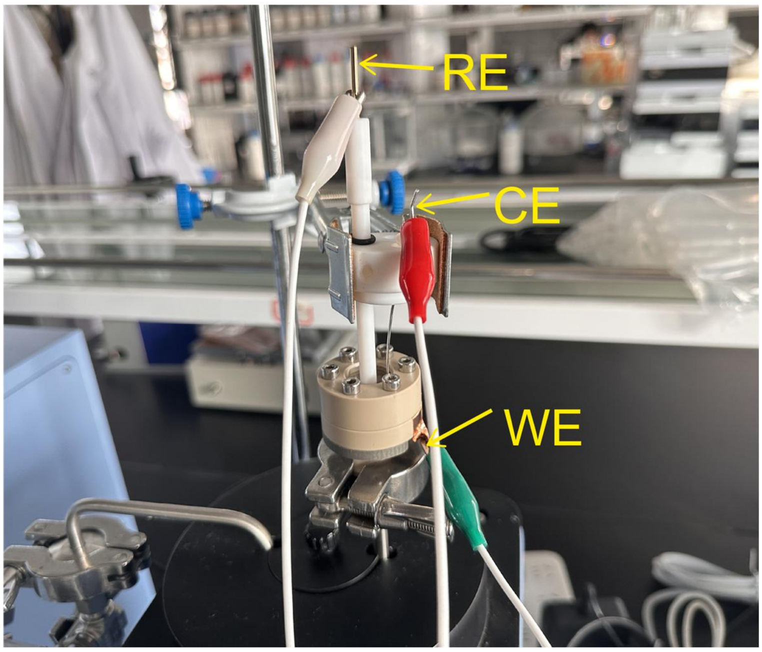

Fig. S34 The setup used for online DEMS experiments.

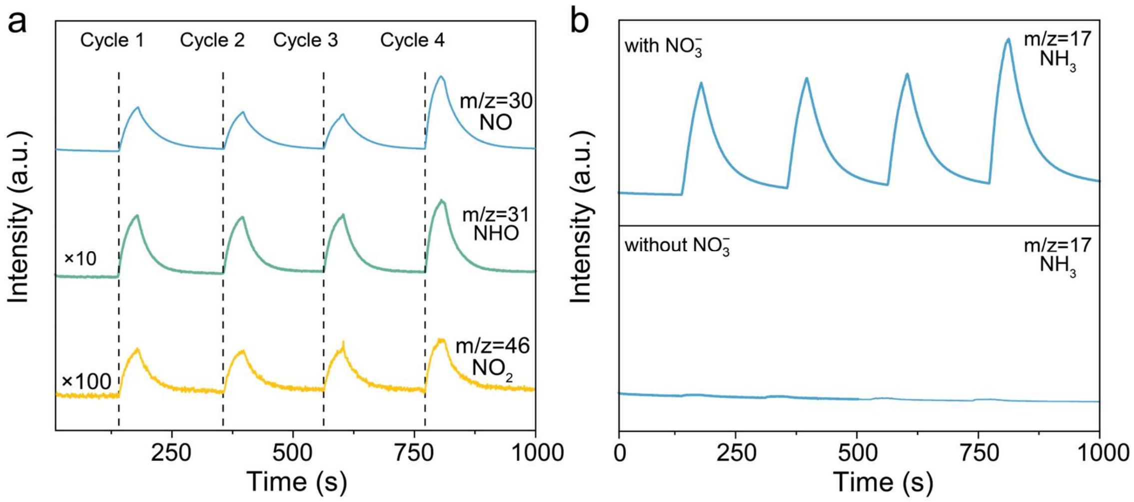

Fig. S35 DEMS analysis of N-containing species generated during NO_3^-RR on Ag_1@Cu_2O NWs. (a) DEMS of the gaseous and volatile N species (NO, NHO, NO_2) generated during NO_3^-RR. (b) DEMS of NH_3 and H_2 signals during tests in 1 M KOH electrolyte with 0.1 M NO_3^-, as well as for NH_3 signal in 1 M KOH electrolyte without 0.1 M NO_3^-.

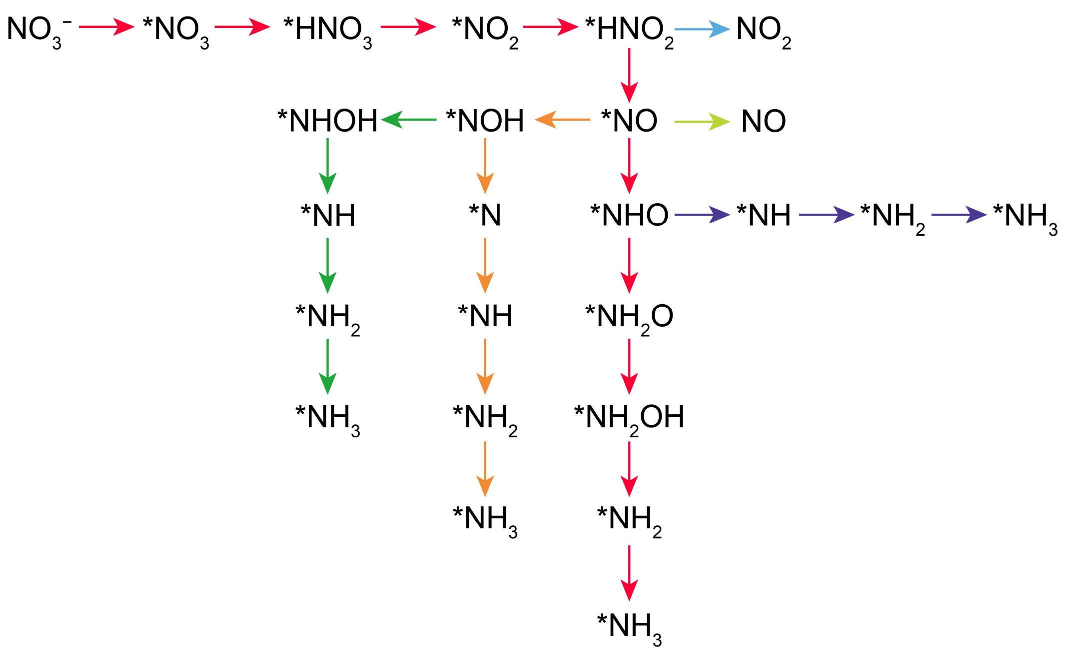

Fig. S36 Overview of reaction pathways of NO_3^-RR for NH_3 synthesis.

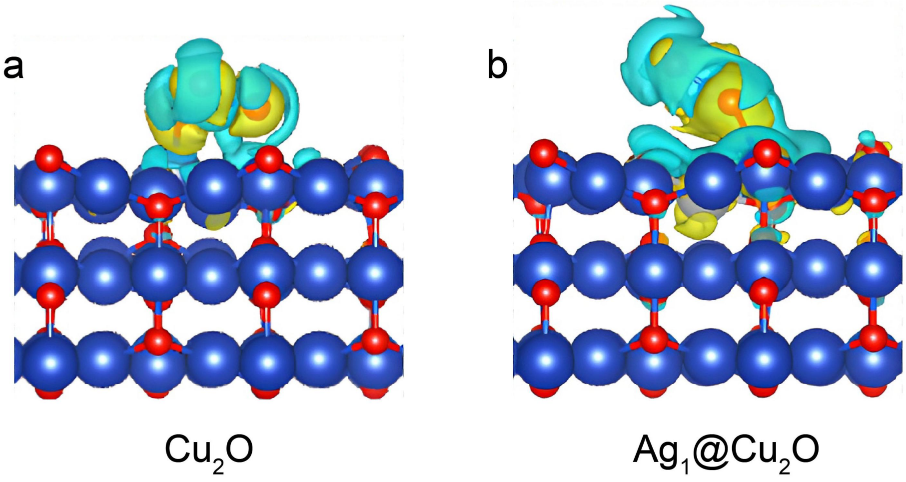

Fig. S37 Differential charge density diagrams after the adsorption of $*NO_3$ on (a) Cu_2O and (b) $Ag_1@Cu_2O$ models. The yellow and cyan surfaces correspond the charge gain and lost regions, respectively.

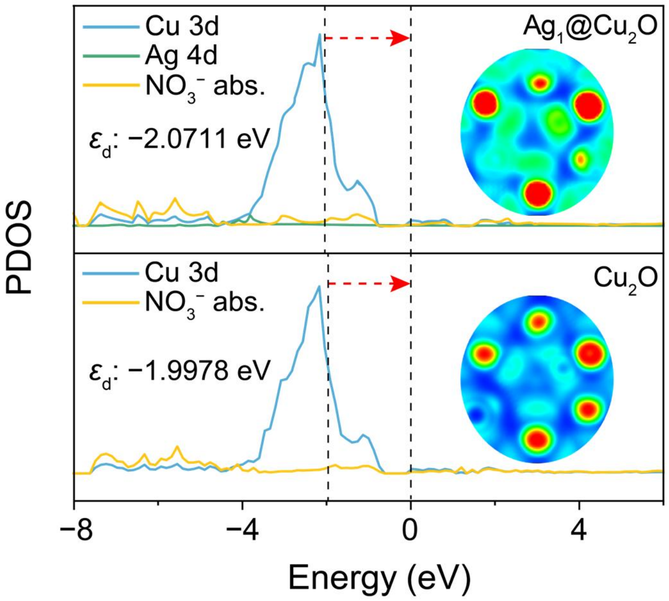

Fig. S38 Calculated PDOS for NO_3^- adsorbed on $Ag_1@Cu_2O$ and Cu_2O.

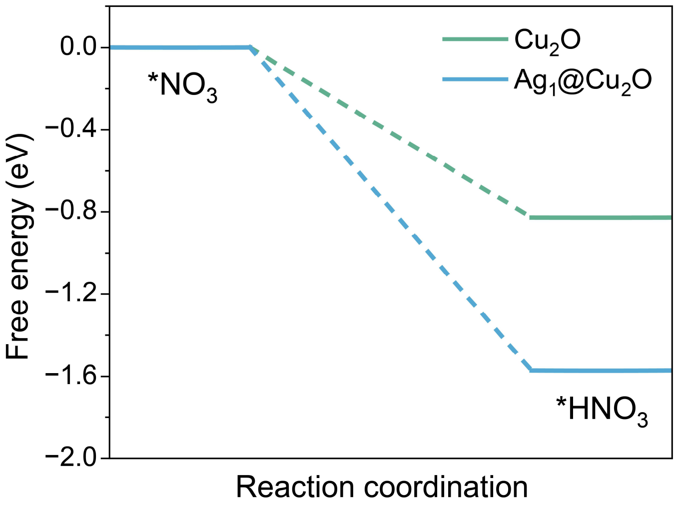

Fig. S39 Free energies of *NO_3 hydrogenation on Cu_2O and $Ag_1@Cu_2O$ models.

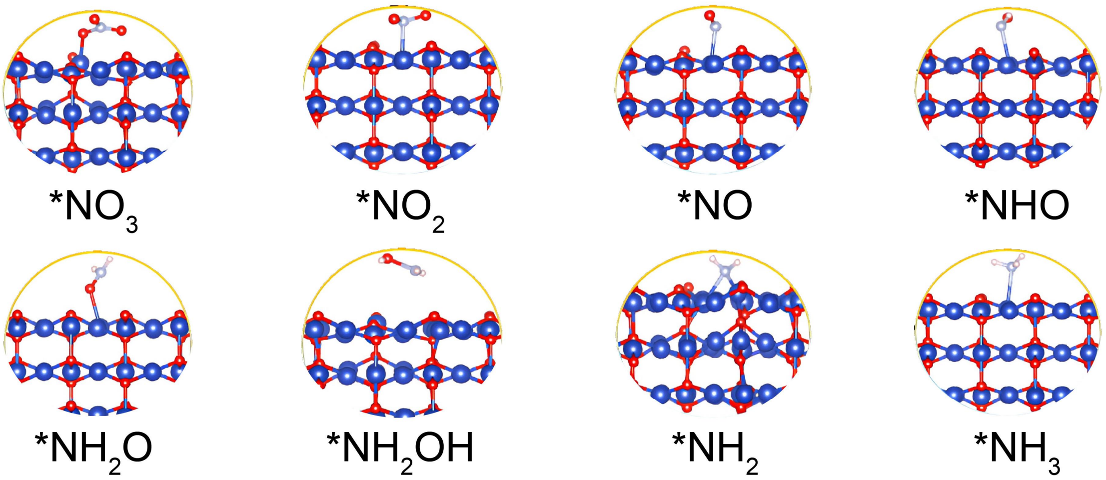

Fig. S40 Atomic configurations of N-containing intermediates adsorbed on Cu_2O model. Blue: Cu; red: O; grey: N; pink: H.

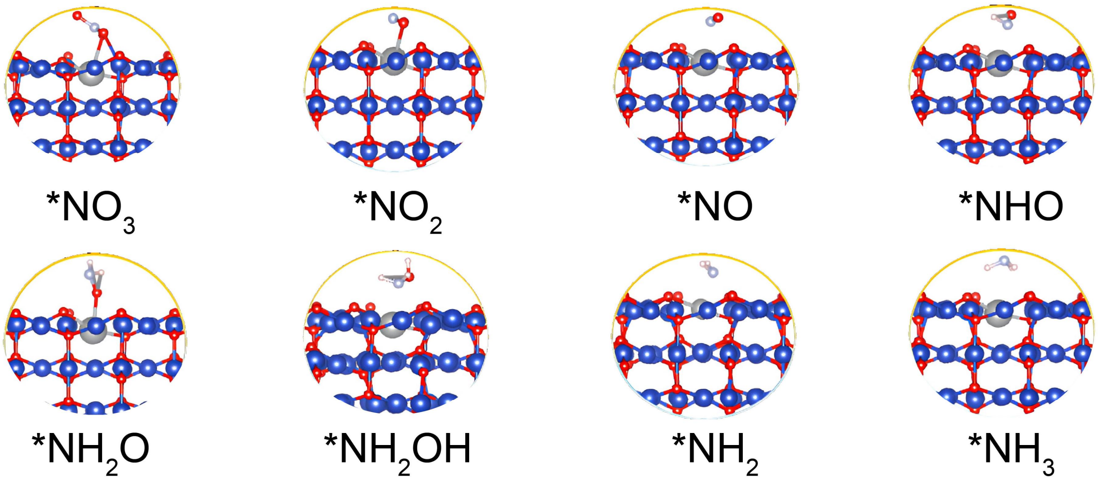

*NO_3 *NO_2 *NO *NHO

*NH_2O *NH_2OH *NH_2 *NH_3

Fig. S41 Atomic configurations of N-containing intermediates adsorbed on $Ag_1@Cu_2O$ model. Silver: Ag; blue: Cu; red: O; grey: N; pink: H.

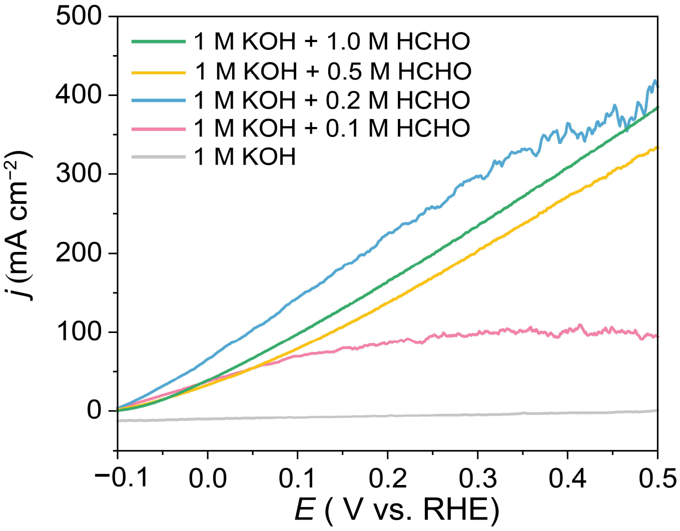

Fig. S42 LSVs of Ag_1@Cu_2O NWs at 5 mV s^{-1} in 1 M KOH with different HCHO concentrations. The higher current density was observed with 1 M KOH and 0.2 M HCHO at the same potential, while further increase in HCHO concentration led to a decrease in current, possibly attributed to the enhanced disproportionation reaction (Cannizzaro reaction) at higher concentrations.[4]

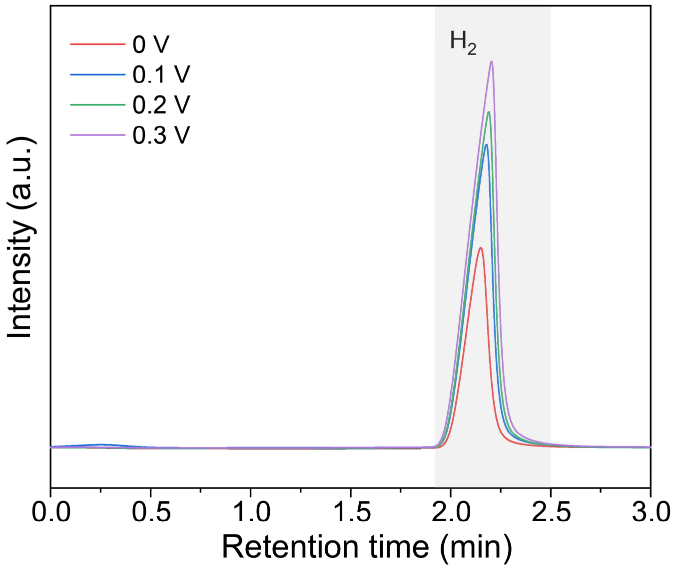

Fig. S43 GC spectra of gaseous H_2 product from FOR on Ag_1@Cu_2O NWs tested over a potential range of 0 to 0.3 V vs. RHE.

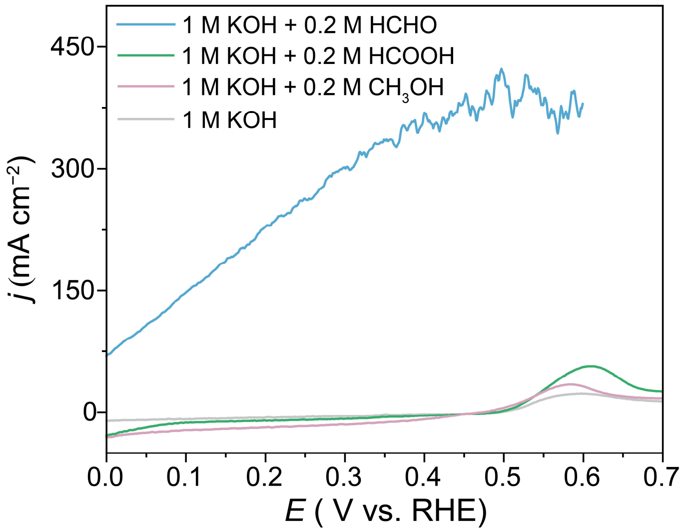

Fig. S44 LSV curves at 5 mV s^{-1} for anodic electrooxidation of HCHO, HCOOH, and CH_3OH on $Ag_1@Cu_2O$ NWs, respectively.

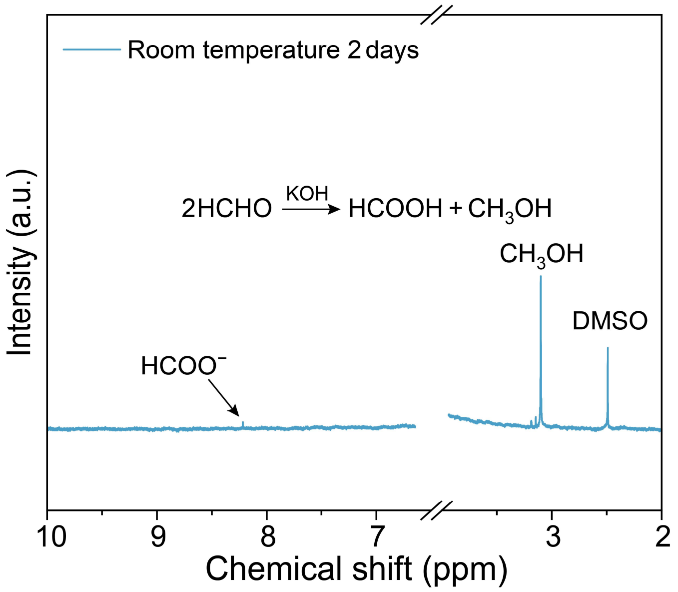

Fig. S45 ^{1}H NMR spectrum of the electrolyte of 1 M KOH and 0.2 M HCHO after two days period without bias. To rule out the influence of non-electrochemical processes in the electrolysis, we analyzed the product composition using ^{1}H NMR spectroscopy of the same electrolyte after it was left to stand at room temperature for two days without bias. In the ^{1}H NMR spectrum, it reveals that the peak intensity corresponding to formate after this duration is negligible. This finding strongly suggests that the formation of formate is primarily a result of the electrocatalytic process.

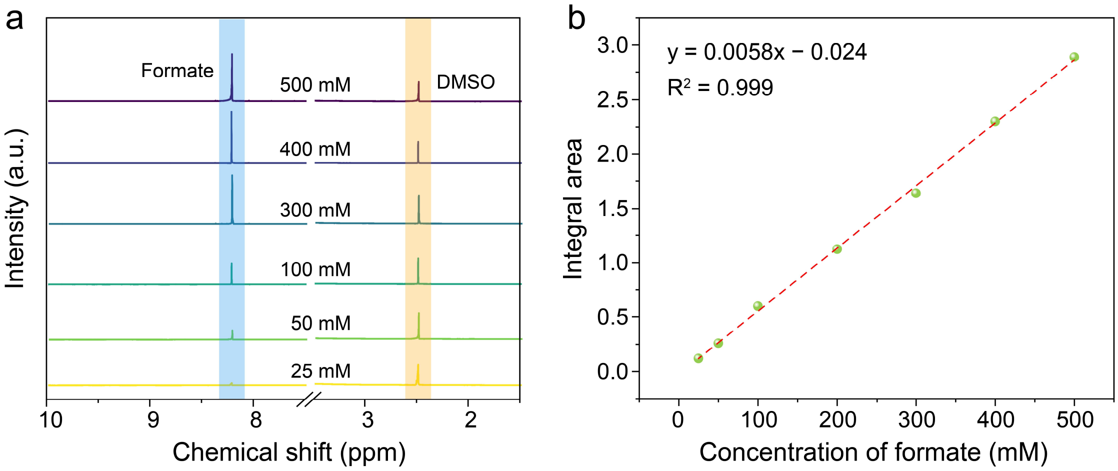

Fig. S46 Standard calibration curve for formate quantification by ^{1}H NMR. (a) ^{1}H NMR spectra of HCOOH at different concentrations; (b) the corresponding standard calibration curve. The concentration of HCOOH can be quantitatively determined by ^{1}H NMR with DMSO as an external standard.

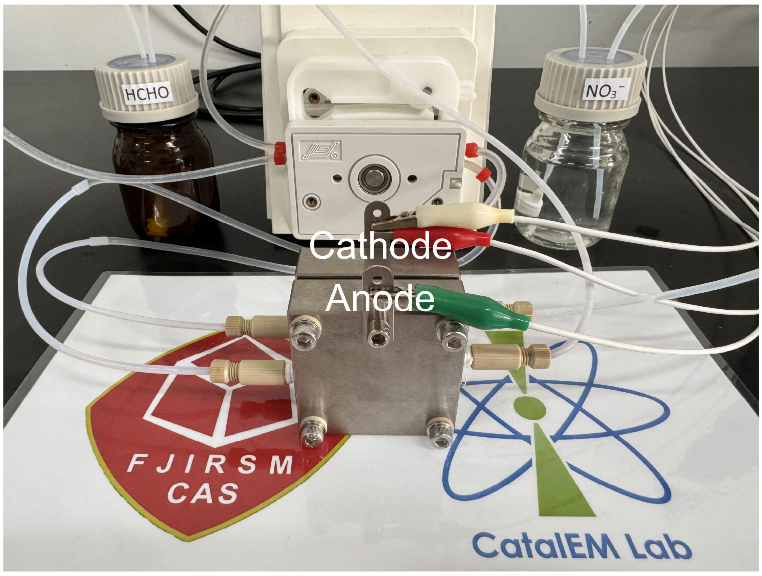

Fig. S47 Photograph of the NO_3^-RR/FOR paired electrolysis in an MEA electrolyzer.

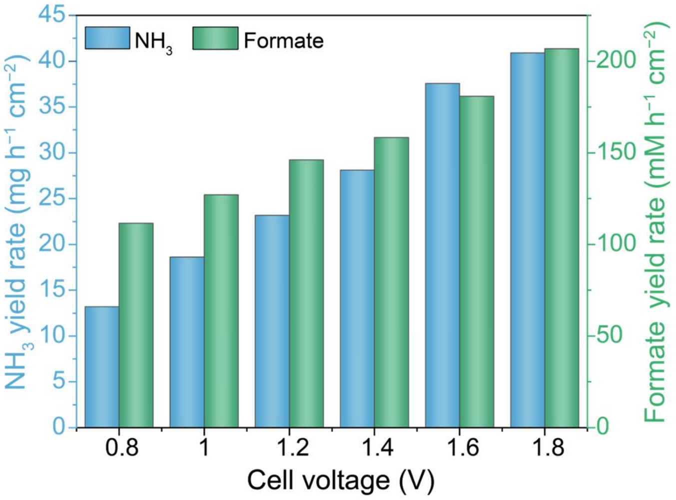

Fig. S48 NH_3 and formate yield rates as a function of cell voltage in NO_3^-RR/FOR MEA electrolysis, respectively.

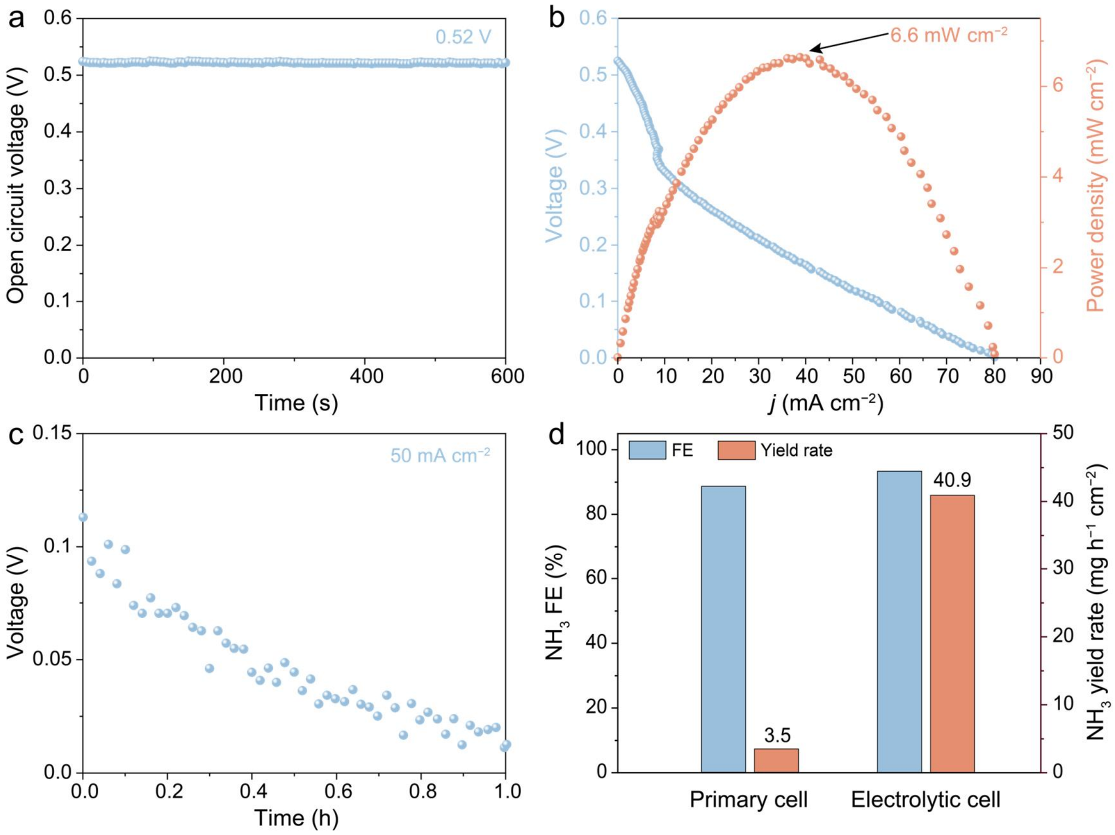

Fig. S49 Performance of the NO_3^-–HCHO primary cell. (a) OCV plot. (b) Discharge and power density curves. (c) *I*–*t* curve at 50 mA cm^{-2} for 1 h. (d) Comparison of NH_3 production performance between the primary cell at the discharging current density of 50 mA cm^{-2} and the MEA electrolyzer at 1.8 V.

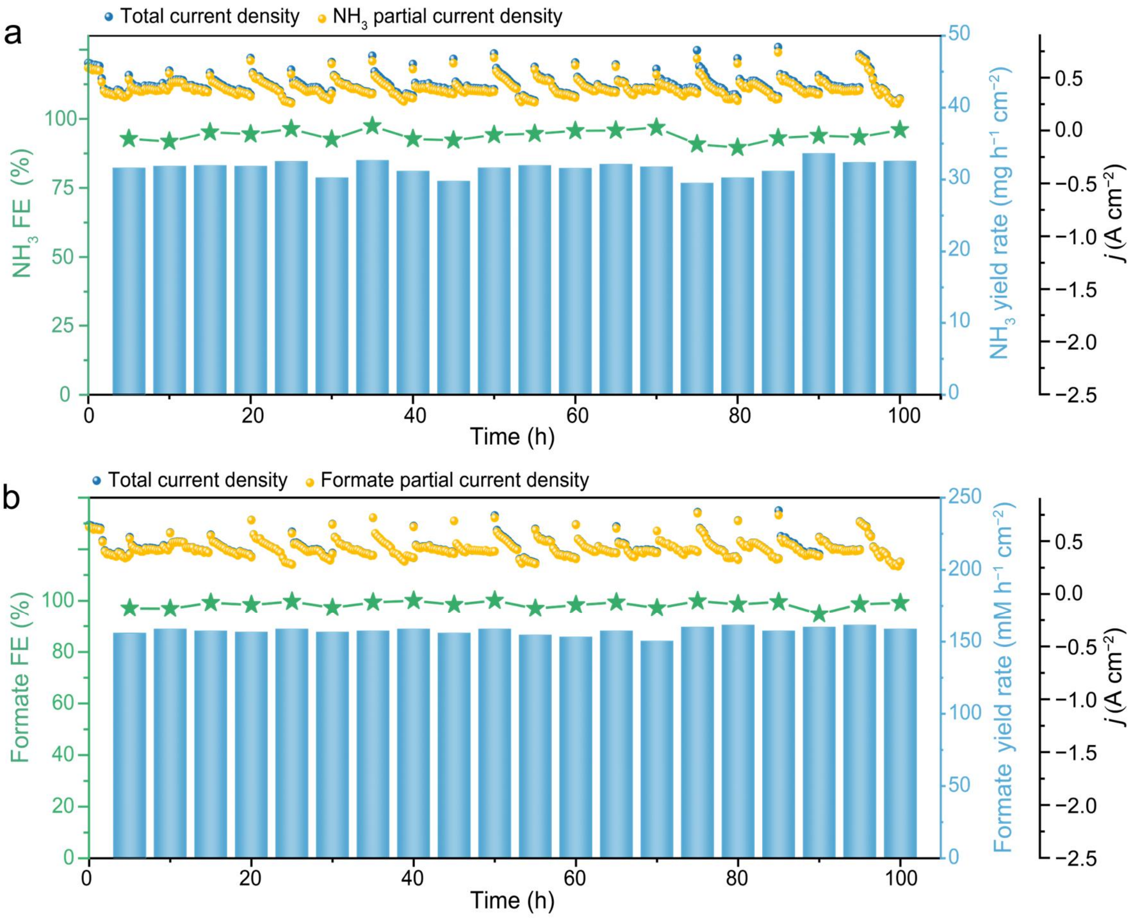

Fig. S50 Current densities, FEs and yield rates of electrolytic products at 1.6 V over the prolonged MEA-based paired NO_3^-RR/FOR electrolysis for 100 h (each cycle lasted for 5 h). (a) NH_3; (b) formate.

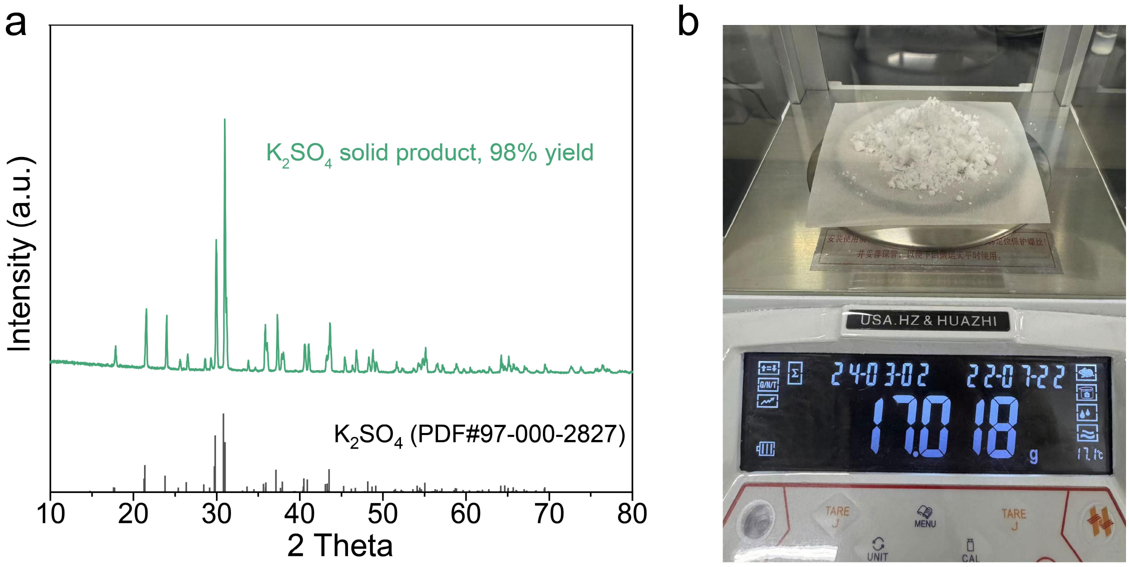

Fig. S51 (a) XRD pattern of the obtained K_2SO_4 byproduct. (b) Digital photo of 17.018 g of the obtained K_2SO_4 byproduct collected from the tandem electrochemical-chemical synthesis.

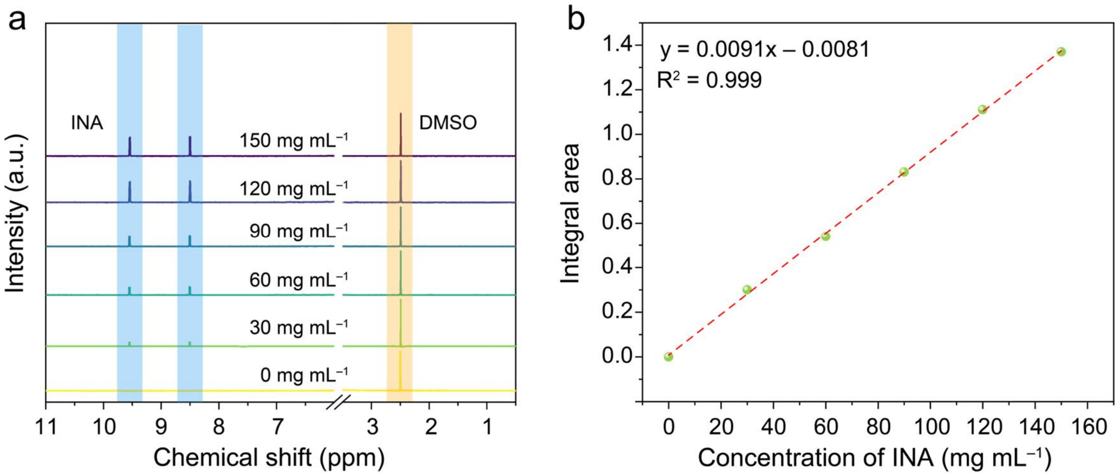

Fig. S52 Standard calibration curve for INA quantification by ^{1}H NMR. (a) ^{1}H NMR spectra of INA at different concentrations; (b) the corresponding standard calibration curve. The concentration of INA can be quantitatively determined by ^{1}H NMR with DMSO as an external standard.

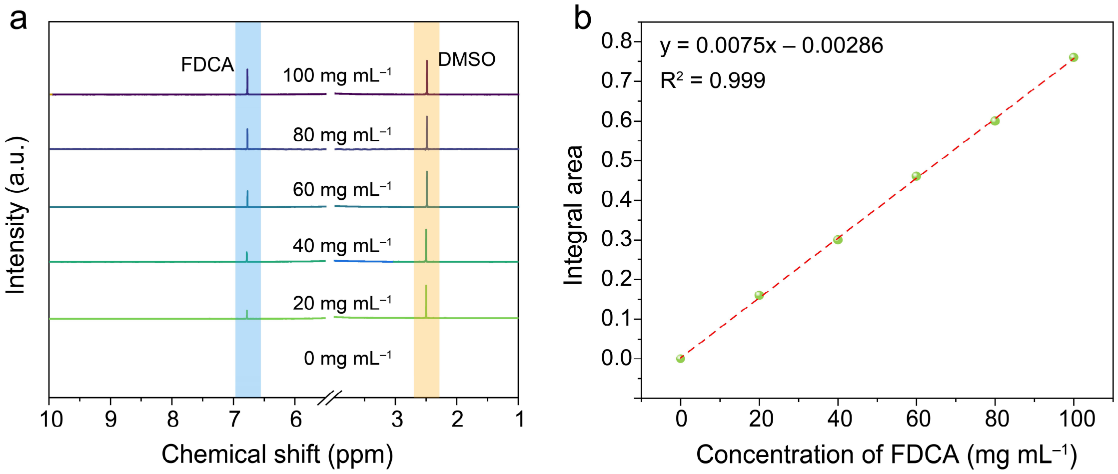

Fig. S53 Standard calibration curve for FDCA quantification by ^{1}H NMR. (a) ^{1}H NMR spectra of FDCA at different concentrations; (b) the corresponding standard calibration curve. The concentration of FDCA can be quantitatively determined by ^{1}H NMR with DMSO as an external standard.

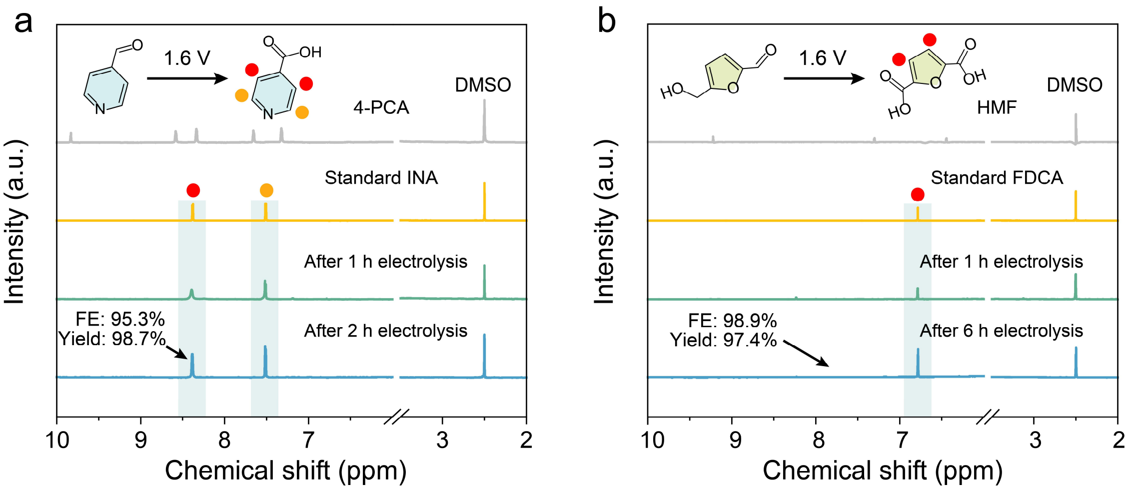

Fig. S54 ^{1}H NMR spectra of the anodic acid products from the paired NO_3^-RR/AOR MEA-based electrolysis. (a) Isonicotinic acid (INA) from NO_3^-RR/4-PCAOR and (b) 2,5-furandicarboxylic acid (FDCA) from NO_3^-RR/HMFOR electrolysis.

Supplementary Note S1

Rough estimate of the cost of the product as well as the revenue based on electrochemical data obtained from our MEA electrolyzer.

To evaluate the economic feasibility of the tandem electrochemical-chemical synthetic system in detail, we have adopted the Sargent Group model for technical and economic analysis.[5] The technoeconomic analysis (TEA), which includes the costs of capital, maintenance, installation, and operation were further introduced to evaluate the contribution of the coupling strategy to the total plant-gate levelized cost. Unless otherwise specified, all currencies are denominated in US dollar ($).

For ammonium formate synthesis from the paired NO_3^-RR/FOR in an MEA-based electrolysis:

Assuming the laboratory production of 10.7 g of ammonium formate is scaled up to 1 ton per day in an industrial setting, the Faradaic efficiency (FE) at both the cathode and anode achieves an optimal value of 96% at a voltage of 1.6 V, with a current density (j) of 600 mA cm^{-2}. In the electrochemical reactions at the cathode and anode, the number of electrons transferred is equivalent, resulting in the production of 8 moles of formic acid for every mole of NH_3 produced. Consequently, to manufacture 1 ton of ammonium formate, a total of 15,873 moles of formate and NH_3 are required, considering an overall yield of 84.8%. Additionally, if both nitrate (NO_3^-) and formaldehyde (HCHO) are sourced from industrial waste, then the cost associated with feedstock sourcing becomes negligible.

1. **Capital cost:**

(1) Cell cost (calculated by the estimated amount of 10,000 $ per square meter):

Cell area S (m^2) = Required current I (A) / Current density j (A m^{-2})

$Q = (n(NH_3) \times N \times F) / (FE \times Y)$

$= (15873 \text{ mol} \times 8 \times 96485 \text{ C mol}^{-1}) / (96\% \times 84.8\%)$

$= 1.51 \times 10^{10}$ C

$I = Q$ / (daily operation time of power plant × capacity factor)

$= 1.51 \times 10^{10} \text{ C} / (21.6 \times 3600 \text{ s} \times 0.9)$

$= 2.15 \times 10^5$ A

Note: The capacity factor is expected to operate on any day, assuming 0.9, which means that the plant will operate for 21.6 hours per day.

Cell cost = $(2.15 \times 10^5 \text{ A} / 6000 \text{ A m}^{-2}) \times 10000 \text{ \$ m}^{-2} = 3.58 \times 10^5$ $

(2) Total cost of catalyst and membrane (assuming 5% of the electrolytic cell cost): 3.58×10^5 \$ × 0.05 = 1.79×10^4 \$

Capital cost = (Cell cost + Total cost of catalyst and membrane) / power plant life (day)

= (3.58×10^5 \$ + 1.79×10^4 \$) / (50 × 365) = 20.6 \$

Note: The life of the power plant is 50 years based on the world average.

2. Maintenance cost:

Capital cost × 10% = 2.06 \$

3. Balance of plant:

Capital cost × BOP index (0.35) = 7.21 \$

4. Installation cost:

Capital cost × Lange coefficient (0.2) = 4.12 \$

5. Power cost:

Power (kWh) = $Q \times E = 1.51 \times 10^{10}$ C × 1.6 V × 10^{-3} / 3600 s = 6711 kWh

Note: The electricity price is 0.03 \$ $(\mathrm{kWh})^{-1}$, referring to the renewable electricity alone price.[6]

Power cost: 6711 kWh × 0.03 \$ $(\mathrm{kWh})^{-1}$ = 201.3 \$

6. Operating cost:

Capital cost × Operating cost (0.1) = 2.06 \$

Note: Assuming 10% of capital cost.

Total cost = Capital cost + Maintenance cost + Balance of plant + Installation cost + Power cost + Operating cost

= 20.6 \$ + 2.06 \$ + 7.21 \$ + 4.12 \$ + 201.3 \$ + 2.06 \$

= 237.4 \$ < 780 \$ (market price of ammonium formate)

Supplementary Tables

Table S1 Market prices of the related several important chemicals.

Chemicals	US$ ton^{-1}
NH_4Cl	132
$(NH_4)_2SO_4$	160
$CO(NH_2)_2$	350
HCOOH	439
Liquid NH_3	453
K_2SO_4	**494**
$HCOONH_4$	**780**

Prices of the chemicals were obtained from website: https://www.sunsirs.com, on Jan. 12, 2024.

Table S2 ICP-OES analysis of $Ag_1@Cu_2O$ NWs before and after the stability test.

$Ag_1@Cu_2O$ NWs	Cu (wt%)	Ag (wt%)
Before stability test	98.19	0.25
After stability test	97.37	0.21

Table S3 Market prices of various metals commonly reported in NO_3^-RR catalysis.

Metal	**US$ g^{-1}**
Rh	155.16
Pd	32.83
Ru	24.59
Ag	**0.81**
Co	0.029
Cu	**0.00842**

The prices for various metals were acquired from website: https://tradingeconomics.com, on January 5, 2024.

Table S4 EXAFS fitting parameters extracted at the Ag *K*-edge for $Ag_1@Cu_2O$ NWs and reference samples.

Element	**Bonding**	***CN***	***R* (Å)**	**σ^2 (Å^2)**	**ΔE_0 (eV)**	**R-factor**
Ag	Ag–O	1.69 ± 0.33	2.24 ± 0.02	0.012	3.87 ± 1.53	0.02
	Ag–Cu	1	2.58 ± 0.03	0.006		

CN: coordination number; *R*: bond distance; σ^2: Debye-Waller factor; ΔE_0: inner potential correction. R factor: goodness of fit. The pretreatment of data was performed using the Athena software, and the EXAFS fittings of the Ag *K*-edge spectra were performed using the Artemis software. Fitting range: *k* ranges from 1−10 Å^{-1} and *R* ranges from 1.3−2.9 Å.

Table S5 Comparison of the electrocatalytic NO_3^--to-NH_3 performance of $Ag_1@Cu_2O$ NWs with other reported electrocatalysts in 1 M KOH solution with varying NO_3^- concentrations.

Catalyst	Nitrate (NO_3^-) concentration	Potential (V vs. RHE)	Peak FE_{NH3}	$j_{max.}$ (mA cm^{-2})	Yield rate (mg_{NH3} h^{-1} cm^{-2})	Ref.
$Ag_1@Cu_2O$ NWs	0.01 M	−0.1	**99.9%**	283.6	3.8	This work
$Ag_1@Cu_2O$ NWs	0.1 M	−0.4	**100%**	1163	40.8	This work
$Ag_1@Cu_2O$ NWs	0.25 M	−0.8	**95.2%**	1744	94.5	This work
$Ag_1@Cu_2O$ NWs	0.5 M	−1.0	**91.2%**	**2320**	**184.4**	This work
$CuCo_2O_4$/Ni	0.2 M	−0.9	96.8%	1384.7	145.8	*Adv. Mater.* 2023[7]
CNS-CoP/Cu foam	1.0 M	−1.03	88.6%	~550	144	*Nat. Commun.* 2022[8]
Ru/Cu_2O	1.0 M	−0.4	75%	2007.5	119	*J. Am. Chem. Soc.* 2023[9]
Co_3O_4/Cu_1-N-C	1.0 M	−1.0	97.7%	~1700	114	*Nat. Commun.* 2024[10]
CuNi NPs/CF	0.715 M	−0.68	97.03%	~1350	94.6	*Energy Environ. Sci.* 2023[11]
0.6W-O-CoP@NF	0.1 M	−0.7	95.2%	~950	88.9	*Adv. Mater.* 2023[12]
$Cu_{50}Co_{50}$	0.1 M	−1.0	~100%	~1000	81.6	*Nat. Commun.* 2022[13]
Ru-Cu NW	0.032 M	−0.2	93%	~1000	76.5	*Nat. Nanotechnol.* 2022[14]
Cu plates	0.5 M	−2.0	99%	900	53.4	*Angew. Chem. Int. Ed.* 2024[15]
$(Co_{0.83}Ni_{0.16})_2Fe$	0.1 M	−0.6	97.8%	~700	50.5	*Angew. Chem. Int. Ed.* 2024[16]
D-$Ni(OH)_2$/Ni@CF	0.1 M	−0.7	98.99%	~560	47.85	*Nat. Commun.* 2024[17]
CNS@CoP	0.1 M	−1.0	95.1%	~450	43.9	*Chem Catal.* 2023[18]
FeB_2	0.1 M	−0.6	96.8%	~322	25.5	*Angew. Chem. Int. Ed.* 2023[19]
CuPd nanocubes	1.0 M	−0.7	92.5%	~400	21.3	*Nat. Commun.* 2022[20]
Fe-cyano-R NSs	0.1 M	−0.6	90.4%	~460	21.1	*ACS Nano* 2022[21]
Mn-$Co(OH)_2$	0.1 M	−1.0	98.9%	~180	19.04	*Angew. Chem. Int. Ed.* 2024[22]
CoP Nas/CFC	1.0 M	−0.5	100%	~440	16.3	*Energy Environ. Sci.* 2022[23]
Pd CuO-200	0.1 M	−0.6	90%	~370	15.7	*Angew. Chem. Int. Ed.* 2024[24]

Table S6 Gibbs free energies of *H intermediate adsorption on $Ag_1@Cu_2O$, Cu_2O, and Cu models, respectively.

Species	**$Ag_1@Cu_2O$**	**Cu_2O**	**Cu**
*****	0	0	0
***H**	0.24	0.33	0.18
H_2	0	0	0

Table S7 Gibbs free energies of NO_3^-RR for different intermediates adsorbed on models of $Ag_1@Cu_2O$ and Cu_2O models, respectively.

Species	**$Ag_1@Cu_2O$**	**Cu_2O**
*****	0	0
***NO_3**	−1.43	−2.51
***NO_2**	−2.00	−1.12
***NO**	−4.27	−4.24
***NHO**	−5.19	−4.42
***NH_2O**	−5.67	−5.05
***NH_2OH**	−5.19	−4.78
***NH_2**	−7.39	−9.49
***NH_3**	−8.79	−8.78
NH_3	−8.39	−8.39

Table S8 Comparison of the electrocatalytic FOR performance for achieving 100 mA cm^{-2} between Ag_1@Cu_2O NWs and previously reported catalysts.

Catalyst	Electrolyte	*E*@100 mA cm^{-2} (V vs. RHE)	Ref.
Ag_1@Cu_2O NWs	1 M KOH + 0.2 M HCHO	**0.042**	This work
Ag_1@Cu_2O NWs	1 M KOH + 0.2 M HCHO	**0.31 V@300 mA cm^{-2}**	This work
Cu_2O	1 M KOH + 0.1 M HCHO	0.238	*Nano-Micro Lett.* 2022[25]
Pd	1 M KOH + 0.6 M HCHO	~0.7	*Nat. Catal.* 2022[4]
Cu_3Ag_7/CF	1 M KOH + 0.6 M HCHO	0.2	*Nat. Commun.* 2023[26]
Cu_xO@CF	1 M KOH + 0.1 M HCHO	~0.17	*Chem* 2023[27]
Cu_2O	1 M KOH + 1.0 M HCHO	~0.3	*Energy Environ. Sci.* 2023[28]
Cu_3Ag_7/CF	1 M KOH + 0.6 M HCHO	~0.27	*Energy Environ. Sci.* 2024[29]

Table S9 Comparison of the actual and theoretical amount of H_2 produced during electrocatalytic FOR on $Ag_1@Cu_2O$ NWs.

Charges (C)	Reaction time (s)	n (mmol)$_{\text{theoretically produced}}$	n (mmol)$_{\text{actually produced}}$
0	0	0.00	0.00
50	215.8	0.26	0.26
100	445	0.52	0.49
150	690.6	0.78	0.76
200	959.4	1.04	1.02
250	1264.9	1.30	1.28
300	1626.6	1.55	1.51
350	2091.8	1.81	1.80
400	2780.2	2.08	2.05
450	3237.3	2.34	2.3

Table S10 Comparison of performance of bifunctional electrocatalysts in alkaline NO_3^-RR-based two-electrode electrolysis using a supporting 1 M KOH or 1 M NaOH for both the catholyte and analyte.

Catalyst	Catholyte	Anolyte	E_{100} (V)	E_{300} (V)	Peak FE_{NH3}	$Yield_{NH3}$ rate (mg h^{-1} cm^{-2})	Ref.
[a]**$Ag_1@Cu_2O$ NWs**	0.1 M KNO_3	0.8 M HCHO	**0.01**	**0.61**	96%	**37.6**	This work
[a]**Ru/Cu_2O**	0.1 M KNO_3	1 M KOH	~2.2	~3	~99%	~17	*J. Am. Chem. Soc.* 2024[9]
[a]**CNs@CoP**	0.1 M KNO_3	0.1 M glycerol	~1.36	~1.6	96.4%	15.2	*Chem Catal.* 2023[18]
[a]**Cu-NiCo/NF**	0.1 M KNO_3	0.1 M glycerol	~1.35	~1.55	–	–	*Angew. Chem. Int. Ed.* 2024[30]
[a]**G-RuCo**	0.6 M KNO_3	1 M KOH	~1.72	~1.8	80%	–	*Nat. Commun.* 2024[31]
[a]**Ru/Cu_2O**	0.1 M KNO_3	1 M KOH	~0.5	~1.4	~87.5%	~18.6	*ACS Energy Lett.* 2024[32]
[b]**Cu_2O**	0.03 M KNO_3	1 M HCHO	~1.3 V@50 mA cm^{-2}		99.77%	2.4	*Energy Environ. Sci.* 2023[28]
[c]**CoP NAs/CFC**	1 M $NaNO_3$ + 0.1 M ph-CH_2OH		~1.64 V@60 mA cm^{-2}		–	–	*Energy Environ. Sci.* 2022[23]

Note: E_{100} and E_{300} represent the cell voltage required for attaining the current densities of 100 and 300 mA cm^{-2}, respectively.

[a] Membrane electrode assembly electrolytic cell.

[b] H-type electrolytic cell.

[c] Single electrolytic cell.

Supplementary Movies

Movie S1 3D electron tomography of a single $Ag_1@Cu_2O$ nanowire.

Movie S2 Paired NO_3^-RR/FOR electrolysis in an MEA-based electrolyzer.

Supplementary notes and references

1. A. Deng, E. Zhao, Q. Li, Y. Sun, Y. Liu, S. Yang, H. He, Y. Xu, W. Zhao, H. Song, Z. Xu and Z. Chen, *ACS Nano*, 2023, **17**, 11869-11881.
2. M. P. Seah, L. S. Gilmore and G. Beamson, *Surf. Interface Anal.*, 1998, **26**, 642-649.
3. X. H. Jiang, L. S. Zhang, H. Y. Liu, D. S. Wu, F. Y. Wu, L. Tian, L. L. Liu, J. P. Zou, S. L. Luo and B. B. Chen, *Angew. Chem. Int. Ed.*, 2020, **59**, 23112-23116.
4. G. Han, G. Li and Y. Sun, *Nat. Catal.*, 2023, **6**, 224-233.
5. W. R. Leow, Y. Lum, A. Ozden, Y. H. Wang, D. H. Nam, B. Chen, J. Wicks, T. T. Zhuang, F. W. Li, D. Sinton and E. H. Sargent, *Science*, 2020, **368**, 1228-1233.
6. S. Han, H. Li, T. Li, F. Chen, R. Yang, Y. Yu and B. Zhang, *Nat. Catal.*, 2023, **6**, 402-414.
7. R. Gao, T. Y. Dai, Z. Meng, X. F. Sun, D. X. Liu, M. M. Shi, H. R. Li, X. Kang, B. Bi, Y. T. Zhang, T. W. Xu, J. M. Yan and Q. Jiang, *Adv. Mater.*, 2023, **35**, e2303455.
8. K. Fan, W. Xie, J. Li, Y. Sun, P. Xu, Y. Tang, Z. Li and M. Shao, *Nat. Commun.*, 2022, **13**, 7958.
9. Q. Hu, K. Yang, O. Peng, M. Li, L. Ma, S. Huang, Y. Du, Z. X. Xu, Q. Wang, Z. Chen, M. Yang and K. P. Loh, *J. Am. Chem. Soc.*, 2024, **146**, 668-676.
10. Y. Liu, J. Wei, Z. Yang, L. Zheng, J. Zhao, Z. Song, Y. Zhou, J. Cheng, J. Meng, Z. Geng and J. Zeng, *Nat. Commun.*, 2024, **15**, 3619.
11. W. Yu, J. Yu, M. Huang, Y. Wang, Y. Wang, J. Li, H. Liu and W. Zhou, *Energy Environ. Sci.*, 2023, **16**, 2991-3001.
12. Z. Chang, G. Meng, Y. Chen, C. Chen, S. Han, P. Wu, L. Zhu, H. Tian, F. Kong, M. Wang, X. Cui and J. Shi, *Adv. Mater.*, 2023, **35**, e2304508.
13. J. Y. Fang, Q. Z. Zheng, Y. Y. Lou, K. M. Zhao, S. N. Hu, G. Li, O. Akdim, X. Y. Huang and S. G. Sun, *Nat. Commun.*, 2022, **13**, 7899.
14. F. Y. Chen, Z. Y. Wu, S. Gupta, D. J. Rivera, S. V. Lambeets, S. Pecaut, J. Y. T. Kim, P. Zhu, Y. Z. Finfrock, D. M. Meira, G. King, G. Gao, W. Xu, D. A. Cullen, H. Zhou, Y. Han, D. E. Perea, C. L. Muhich and H. Wang, *Nat. Nanotechnol.*, 2022, **17**, 759-767.
15. L. Zhou, X. Chen, S. Zhu, K. You, Z. J. Wang, R. Fan, J. Li, Y. Yuan, X. Wang, J. Wang, Y. Chen, H. Jin, S. Wang and J. J. Lv, *Angew. Chem. Int. Ed.*, 2024, **63**, e202401924.
16. <*Angew Chem Int Ed*, 2024 DOI: 10.1002/anie.202400428.
17. J. Lv, A. Cao, Y. Zhong, Q. Lin, X. Li, H. B. Wu, J. Yan and A. Wu, *Nat. Commun.*, 2024, **15**.
18. J. Li, H. Li, K. Fan, J. Y. Lee, W. Xie and M. Shao, *Chem Catal.*, 2023, **3**, 100638.
19. G. Zhang, X. Li, K. Chen, Y. Guo, D. Ma and K. Chu, *Angew. Chem. Int. Ed.*, 2023, **62**, e202300054.
20. Q. Gao, H. S. Pillai, Y. Huang, S. Liu, Q. Mu, X. Han, Z. Yan, H. Zhou, Q. He, H. Xin and H. Zhu, *Nat. Commun.*, 2022, **13**, 2338.
21. Z. Fang, Z. Jin, S. Tang, P. Li, P. Wu and G. Yu, *ACS Nano*, 2022, **16**, 1072-1081.
22. S. Liang, X. Teng, H. Xu, L. Chen and J. Shi, *Angew. Chem. Int. Ed.*, 2024, **63**, e202400206.
23. S. Ye, Z. Chen, G. Zhang, W. Chen, C. Peng, X. Yang, L. Zheng, Y. Li, X. Ren, H. Cao, D. Xue, J. Qiu, Q. Zhang and J. Liu, *Energy Environ. Sci.*, 2022, **15**, 760-770.
24. Y. Liu, Z. Zhuang, Y. Liu, N. Liu, Y. Li, Y. Cheng, J. Yu, R. Yu, H. Li and D. Wang, *Angew. Chem. Int. Ed.*, 2024, DOI: 10.1002/anie.202411396, e202411396.
25. M. Li, T. Wang, W. Zhao, S. Wang and Y. Zou, *Nano-Micro Lett.*, 2022, **14**, 211.
26. G. Li, G. Han, L. Wang, X. Cui, N. K. Moehring, P. R. Kidambi, D. E. Jiang and Y. Sun, *Nat. Commun.*, 2023, **14**, 525.
27. Y. Pan, Y. Li, C.-L. Dong, Y.-C. Huang, J. Wu, J. Shi, Y. Lu, M. Yang, S. Wang and Y. Zou, *Chem*, 2023, **9**, 963-977.
28. L. Xiao, W. Dai, S. Mou, X. Wang, Q. Cheng and F. Dong, *Energy Environ. Sci.*, 2023, **16**, 2696-2704.
29. L. Zhao, Z. Lv, Y. Shi, S. Zhou, Y. Liu, J. Han, Q. Zhang, J. Lai and L. Wang, *Energy Environ. Sci.*, 2024, **17**, 770-779.
30. C. Li, H. Li, B. Zhang, H. Li, Y. Wang, X. Wang, P. Das, Y. Li, X. Wu, Y. Li, Y. Cui, J. Xiao and Z. S. Wu, *Angew. Chem. Int. Ed.*, 2024, DOI: 10.1002/anie.202411542, e202411542.
31. X. Chen, Y. Cheng, B. Zhang, J. Zhou and S. He, *Nat. Commun.*, 2024, **15**, 6278.
32. Q. Hu, O. Peng, J. Liu, D. Chen and K. P. Loh, *ACS Energy Lett.*, 2024, **9**, 2303-2309.